Research Square

Preprints are preliminary reports that have not undergone peer review.
They should not be considered conclusive, used to inform clinical practice,
or referenced by the media as validated information.

Cellular and spatial continuum of TAM functional states governs immune exclusion and dictates immune checkpoint resistance in melanoma

Sajib Chakraborty
University Medical Center Freiburg
Eyleen Corrales
University Medical Center Freiburg
Ira Godbole
University Medical Center Freiburg
Nawal Madkhali
University of Freiburg
Tonmoy Das
University Medical Center Freiburg
Christopher Krolla
University Medical Center Freiburg
Alexander Nystroem
University Medical Center Freiburg
Frank Meiss
University Medical Center Freiburg
David Rafei
University Medical Center Freiburg
Bertram Bengsch
University Medical Center Freiburg
Geoffroy Andrieux
University Medical Center Freiburg
Melanie Boerries
melanie.boerries@uniklinik-freiburg.de
University Medical Center Freiburg

Research Article

Keywords: Melanoma, Immunotherapy, Lipid-associated TAM, Spatial-transcriptomics, Imaging mass cytometry

Posted Date: June 3rd, 2026

DOI: https://doi.org/10.21203/rs.3.rs-9692259/v1

License: This work is licensed under a Creative Commons Attribution 4.0 International License.
Read Full License

Additional Declarations: No competing interests reported.

Abstract

Background

Immune checkpoint inhibitor (ICI) therapy has transformed melanoma treatment, yet many patients either fail to respond or develop resistance after an initial response. The cellular and spatial determinants within the tumor microenvironment (TME) that underlie these divergent ICI therapy outcomes remain poorly defined. Here, we aimed to characterize the immune composition and spatial organization of the TME associated with ICI response and resistance.

Methods

We integrated public scRNA-seq data (N = 32) with in-house spatial transcriptomics and imaging mass cytometry from an independent melanoma cohort (N = 6) to achieve high-resolution spatial profiling of the tumor microenvironment. This multimodal approach allowed us to map cellular heterogeneity within discrete spatial neighborhoods. To validate our findings, we constructed a scRNA-seq derived signature-matrix and deconvoluted a bulk RNA-seq cohort (N = 334). Clinical associations were assessed using Kaplan–Meier survival analysis, Cox hazards models, and a machine-learning classifier.

Results

We identified a distinct tumor-associated macrophage (TAM) state, termed lipid-associated TAMs (LA-TAMs), characterized by conserved lipid metabolic programs and tumor-specific adaptations in glycolysis under hypoxic conditions. Deep spatial multi-omics profiling revealed divergent immune-architectures associated with treatment outcomes. In Non-Responders, LA-TAMs colocalized with sparsely distributed TIM3^{+} exhausted CD8^{+} T cells within an immune-excluded TME. In contrast, Responder TMEs harbored interferon-primed CCL4^{+} TAMs (IFN-TAMs) spatially associated with Granzyme B^{+} activated CD8^{+} T cells, reflecting an immune-active microenvironment. These findings define contrasting macrophage-centered immune neighborhoods linked to ICI response. Interestingly, patients with LA-TAM–enriched neighborhoods were consistently non-responders or progressed during follow-up, irrespective of the presence of IFN-TAM neighborhoods. Lastly, we constructed a single-cell–derived signature matrix that estimates TAM fractions from bulk RNA-seq data and revealed LA-TAM abundance as a robust, independent predictor of poor ICI response and survival in a validation cohort.

Conclusions

Our study defines the spatial- and metabolic-landscapes of TAM-heterogeneity in melanoma and identifies LA-TAM neighborhoods as a key determinant of ICI resistance. Although patients span a continuum of TAM-centered immune states, the presence of LA-TAM overrides the beneficial effects of

IFN-TAM–associated immune activation. Finally, our proposed Melanoma-TME–derived signature-matrix provides a translatable framework to robustly predict ICI response and resistance.

Background

Melanoma, an aggressive type of skin cancer, can metastasize rapidly if left untreated. Immune checkpoint inhibitor (ICI) therapy is a promising avenue in cancer treatment that has shown significant efficacy in melanoma management. The outcomes of immunotherapy in melanoma treatment have been remarkable for many patients, leading to prolonged survival rates and even complete remission in a fraction of patients [1]. However, not all patients respond equally to immunotherapy. Approximately 40%-50% of patients with metastatic melanoma exhibit an optimal response to ICIs (Responders) such as ipilimumab (anti-CTLA4) or nivolumab (anti-PD-1), whereas the remaining 50–60% patients either do not respond (Non-Responders) or develop resistance over time [2].

Although some underlying mechanisms related to the pharmacodynamics of T-cell invigoration during melanoma immunotherapy have been clarified [3], T-cell–centric models alone do not fully explain the variability in patient responses, and the determinants of poor response to ICI therapies remain incompletely understood. A recent study linked the balance of two $CD8^+$ T cell states, particularly $TCF7^+CD8^+$ cells, to tumor regression and favorable ICI response [4]. Furthermore, another study found that MHC-II^+ melanoma cells can activate $CD4^+$ and $CD8^+$ T cells, which correlates with better ICI outcomes [5]. Although these results reveal important, context-dependent associations between specific cellular states and therapeutic outcomes, they fail to explain the significant heterogeneity in ICI responses across patients.

Additional factors, such as tumor mutational burden, PD-L1 expression, gut microbiota composition, and specific genetic alterations like BRAF-V600E mutations, have been proposed to influence immunotherapy outcomes in melanoma [6]. However, they fail to fully account for the observed variations in patient responses. Moreover, Tirosh *et al.* used single-cell transcriptomics (scRNA-seq) to show that melanoma tumors exhibit a complex cellular ecosystem, with distinct transcriptional cell states coexisting within the tumor microenvironment (TME) [7]. This pronounced intratumoral heterogeneity adds an additional layer of complexity, as diverse tumor states and their interactions with the immune compartment can differentially shape responses to immune checkpoint inhibition. Consequently, despite its success, challenges persist in optimizing immunotherapy for melanoma, such as identifying biomarkers to predict treatment response, overcoming resistance mechanisms, and effectively managing immune-related toxicities [8]. Addressing these challenges is crucial to further enhancing the effectiveness and safety of immunotherapy in melanoma treatment.

The lack of predictive markers is particularly concerning given the risk of severe and sometimes irreversible immune-related adverse events [9]. Without the ability to stratify patients based on likely therapeutic outcomes, clinicians lack clear guidance for making individualized treatment decisions. A key obstacle to progress is our incomplete understanding of how the tumor microenvironment (TME)

differs between Responders and Non-Responders, in terms of both cellular composition and spatial organization. Growing evidence suggests that, in addition to the abundance of immune cells, spatial immune architecture critically shapes local immunoregulation and influences response to ICIs [10].

While previous studies have emphasized adaptive immunity, the role of innate immune cells remains understudied. Among immune components within the TME, tumor-associated macrophages (TAMs) have emerged as important regulators of immune suppression and therapeutic resistance [11]. TAMs are often the most abundant immune population within the TME, and their abundance is increasingly leveraged as a diagnostic marker due to its association with patient prognosis [12]. A recent analysis of public scRNA-seq data revealed that ICI Non-Responders melanoma patients harbor immunosuppressive TREM2$^+$ TAMs [13]. Despite these findings, spatial context is lacking, which limits the identification of precise cellular neighborhoods that modulate the response to ICI within the tumor. Investigating the spatial organization and interactions of TAMs and CD8$^+$ T cells within the TME could provide deeper insights into ICI responses and support the development of predictive biomarkers. Recent studies on metabolic and inflammatory diseases have described a specialized subset of macrophages, lipid-associated macrophages (LAMs), characterized by the expression of TREM2, APOE, CD9, and CD36, which mediate lipid scavenging and tissue remodeling [14]. However, it is unclear whether a functionally analogous TAM population exists within the melanoma microenvironment and how such TAMs contribute to ICI resistance.

To address the current challenges, we investigated the heterogeneity of TAMs, tumors, and CD8$^+$ T cells within the TME of melanoma patients undergoing ICI therapy. Using integrated single-cell analysis, coupled with deep spatial profiling through spatial-transcriptomics and imaging mass cytometry (IMC), we uncovered the preferential occurrence of opposing TAM states in the TME of ICI therapy Non-Responder and Responder melanoma patients. Spatial muti-omics analysis unveiled contrasting TME architectures in Non-Responder and Responder patients, in which distinct TAM states interact with CD8$^+$ T cells to induce a spatial context-dependent immunosuppressive or immune-active microenvironment. These findings highlight the pivotal role of spatial immune organization in shaping ICI outcomes, where interactions among different compartments dictate the formation of immunosuppressive or immune-activating neighborhoods. Finally, we validated our findings in a large cohort, establishing the association of TAM states with poor ICI response and demonstrating that TAM fractions serve as robust predictors of ICI outcomes.

Methods

Sources of gene signatures defining distinct states of immune and melanoma cells

Gene signatures defining different states of tumor-associated macrophages (TAMs) based on single-cell RNA-seq (scRNA-seq) data were retrieved from Ma *et al.*[15]. This includes gene signatures of seven

TAM subsets: interferon-primed TAMs (IFN-TAMs), immune regulatory TAMs (Reg-TAMs), inflammatory cytokine-enriched TAMs (Inflam-TAMs), lipid-associated TAMs (LA-TAMs), pro-angiogenic TAMs (Angio-TAMs), RTM-like TAMs (RTM-TAMs), and proliferating TAMs (Prolif-TAMs). Distinct states of $CD8^+$ T cells in melanoma were obtained from Sade-Feldman *et al.*[4], where they utilized transcriptome profiles of 16,291 $CD45^+$ immune cells from 48 tumor samples of melanoma patients treated with checkpoint inhibitors. Gene signatures defining the diverse states of melanoma cells were retrieved from Tsoi *et al.* [16], where the authors performed hierarchical clustering on the expression profiles from a panel of 53 human melanoma cell lines, including paired acquired resistance sublines, established from patient biopsies.

Single-cell transcriptome analysis of human and mouse cells

Firstly, a single-cell RNA sequencing (scRNA-seq) dataset from Sade-Feldman *et al.* [4] representing a dataset representing $CD45^+$ Immune cells (N = 16,291) from 32 patients with available ICI response outcome was obtained and subsequently analyzed with the Seurat R package version 4.3 [17]. Briefly, the population (N = 1377) was retrieved from the $CD45^+$ immune cells and analyzed by dimension reduction based on the manifold learning method (UMAP) as implemented in Seurat. The Louvain clustering followed by differential gene expression analysis was performed. Secondly, we obtained scRNA-seq data from Tirosh *et al.* [7]. Briefly, scRNA-seq profiles representing malignant, stromal, and immune cells (N = 4645) isolated from 19 human melanoma tumor samples were obtained. We then specifically focused on the malignant and macrophage population (N = 1788) and performed UMAP analysis followed by Louvain clustering of the cells using the Seurat package as described above.

Single-cell-wise gene signature enrichment analysis on scRNA-seq data

To estimate the scores for gene signature enrichment in the single-cell datasets, the UCell R-package [18] was utilized. Briefly, based on the Mann–Whitney U statistic, the UCell R-package allows for the estimation of single-cell–wise signature scores called “UCell scores” for the gene sets representing different states of TAMs as reported by Ma *et al.* [15] across the single cells from melanoma patients (Cohort from Sade-Feldman *et al.*) [4]. Similarly, Ucell enrichment analysis for the TAM states was additionally conducted on the single-cell dataset from Tirosh *et al.* [7]

Spatial transcriptomics (stRNA-seq) analyses of tissue samples from metastatic melanoma patients

For Spatial transcriptomics (stRNA-seq) analyses, we enrolled patients with pathologically diagnosed metastatic melanoma (N = 6) at the Clinic of Dermatology and Venerology, University Hospital Freiburg (UKF). The study was approved (24-1387-S1) by the Ethics Committee of the University of Freiburg, and

written informed consent was obtained from all participants prior to inclusion. Formalin-fixed and paraffin-embedded (FFPE) tissue samples were collected from the patients, where three of them were ICI therapy Non-Responders (UKF#1, UKF#2, UKF#3) and the remaining three were Responders (UKF#4, UKF#5, UKF#6). Libraries were prepared from 5 mm diameter, 5 µm-thick tumor-TME interphase tissue sections using Visium Spatial Gene Expression Kit for FFPE (10x Genomics, Pleasanton, CA, USA), according to the instructions from the manufacturer. Paired-end sequencing (2 × 100 bp) on NovaSeq 6000 instrument (Illumina) was carried out at the Genomics and Proteomics Core Facility of the DKFZ, Heidelberg.

Space Ranger analysis pipelines were used to process 10x Genomics Visium data with Hematoxylin and Eosin (H&E) stained images, allowing to mapping of the whole transcriptome in melanoma section tissues. Briefly, the application of the Space Ranger pipeline resulted in a gene count matrix and a spatial information file containing the x and y position and the H&E image. The Space Ranger output was then imported to the SPATA 2.0 package via the Seurat 5.0 package. During the import, firstly, the gene expression was normalized, where the values of each spot were divided by the total number of transcripts and multiplied by 10,000, followed by Log2 transformation. For downstream spatial analysis, we used the SPATA 2.0 package [19]. Briefly, the scaled gene expression values were used to plot single genes or gene signature scores, using the 0.5 quantiles of a probability distribution fitting. The x-axis and y-axis coordinates are given by the input file based on the localization at the H&E staining. We computed a matrix based on the maximum and minimum extension of the spots used (32 × 33), containing the gene expression or combined scores. The data are illustrated as surface plots by the SPATA 2.0 package. Spatial clustering was performed using the BayesSpace Clustering algorithm as implemented in SPATA 2.0. Surface plotting, allowing the visualization of the gene expression of the barcode spots with a spatial dimension, was used, where the x-esthetic and y-esthetic of the plot are mapped onto the respective coordinate variable. Differential expression analysis (DEA) was performed among the spatial clusters.

Spatial neighborhood analysis

We performed spatially Functional Neighborhood Analysis by using pre-existing established gene signatures representing TAM (LA-TAM and IFN-TAM), T-cell (Exhausted-CD8, Activated-CD8, and Memory-effector T cells), and melanoma (Transitory Melanocytic, Melanocytic, Transitory, Neural Crest-like) states. The enrichment scores of individual spots were calculated using the consensus of two common gene-set enrichment algorithms (Over-representation analysis: ORA and Univariate Linear Model: ULM). A 250 µm range of effective paracrine cell-to-cell communication [20] was considered as a functional neighborhood region to calculate rank sums of local neighborhoods normalized for the neighborhood size. For each gene set, the top-enriched spots were selected to estimate the spatial co-localization.

Mixed-effects modeling of gene-set activity within spatially confined regions

Gene-set activity scores were quantified for each spot and compared between experimental conditions using a linear mixed-effects model to account for the non-independent structure of spots originating from the same biological sample. For each gene set, we fitted the model

$$Y_{ij} = \beta_0 + \beta_1 Condition_{ij} + (1|Sample_j)$$

where Y_ij denotes the gene-set activity score of spot i from sample j, β_0 represents the mean gene-set activity for the reference condition, and (1|Sample_ij) represents a random intercept capturing sample-specific variation. The fixed effect β_1 estimates the mean difference in gene-set activity between conditions while adjusting for within-sample correlation. Models were fitted using the lme4 framework. Significance of the condition effect was assessed via t-tests, and p-values were adjusted for multiple testing using the Benjamini–Hochberg procedure.

Ligand-receptor-based interaction analysis among diverse cell types in melanoma tumor microenvironment

The ligand-receptor-based interactions between the TAM, CD8, and melanoma states were explored by using the CellChat [21]. We applied the CellChat R package to explore the global communication among different cell types in melanoma TME. Briefly, the CellChat package was used to quantitatively infer and analyze intercellular communication networks across stRNA-seq datasets from the UKF melanoma cohort (N = 6). CellChat predicts major signaling inputs and outputs for cells and how those cells and signals coordinate functions using network analysis and pattern recognition approaches.

Imaging Mass Cytometry (IMC) sample preparation and data acquisition

Imaging mass cytometry (IMC) was performed on formalin-fixed, FFPE tumor tissue sections from the same cohort used for spatial transcriptomics, consisting of six metastatic melanoma patients, including three ICI Responders and three Non-Responders. Tissue sections (5 µm-thick) were mounted onto silane-coated glass slides and deparaffinized using a xylene and ethanol gradient. Antigen retrieval was performed using Tris-EDTA buffer (pH 9.0) at 95°C for 20 min. The slides were then blocked with 3% bovine serum albumin (BSA) and incubated with a panel of metal-tagged antibodies overnight at 4°C.

IMC antibody panel design

A custom antibody panel was designed to detect immune, stromal, and tumor markers, including CD8a, PD-1, PD-L1, TIM3, Lag-3, Granzyme B (GZMB), CD68, CD163, TREM2, APOE, and melanoma-associated

markers (MITF, S100B, MLANA). All antibodies were conjugated to distinct metal isotopes using the Maxpar® antibody labeling kit (Fluidigm) and validated on control FFPE tissue sections before experimental use.

Imaging and data acquisition

IMC imaging was performed using a Hyperion Imaging System (Fluidigm). Regions of interest (ROIs) were selected based on H&E staining and scanned at a resolution of 1 µm per pixel. Laser ablation was performed at a frequency of 200 Hz, and ion signals were detected using a time-of-flight mass spectrometer. Each acquired image was processed and normalized using the CyTOF software (Fluidigm) to correct for detector sensitivity and isotope spillover.

Single-Cell segmentation and phenotyping

For automated single-cell segmentation and annotation, we employed the IMC-R pipeline, integrating multiple computational tools to ensure accurate identification and classification of cells. Steinbock [22] was utilized for image preprocessing, including background correction, intensity normalization, and channel alignment. Single-cell segmentation was performed using CellProfiler [23], applying a marker-guided approach based on nuclear (e.g., Histone H3) and membrane (e.g., CD45, PanKeratin) staining. Next, the DeepCell Python package [24] is used to run Mesmer, a deep learning-enabled segmentation algorithm pre-trained on TissueNet, to automatically obtain cell masks without any further user input. Cell classification was automated using Penguin [25], which assigned cells to distinct functional states based on predefined marker expression thresholds using a random forest classification algorithm. Quality control measures were applied to filter out artifacts and misclassified cells.

Spatial proteome analysis and neighborhood quantification

For pixel-level visualization, the cytomapper Bioconductor package [26], supporting handling and visualizations of multi-channel images were used. The imcRtools package was used for downstream analysis, including phenograph clustering and spatial neighborhood analysis [22].

Retrieval of bulk RNA-seq data from different cohorts of melanoma patients

We obtained bulk RNA-seq data of melanoma patients (N = 334) from six different cohorts (Hugo *et al.* [27], Riaz *et al.* [28], Van-Allen *et al.* [29], Liu *et al.* [30], Gide *et al.* [31], MGH [32]) for which response outcomes ICI therapy were available. Bulk RNA-seq data were collected from pre-treated melanoma patients, hence herein called “pre-ICI Cohort”. The data were normalized and batch-corrected as described by Freeman *et al.*[33]. Clinicopathological and treatment parameters for the pre-ICI Cohort, including response outcomes and ICI therapy types are given in Supplementary Additional file 8: Table S7. The response outcomes of patients reported in each study were discretized to obtain the binary classification of Non-Responder and Responder as described by Freeman *et al.* [33]

Deconvolution of bulk RNA-seq data from metastatic melanoma patients through CIBERSORTx

The CIBERSORTx algorithm was utilized to process bulk RNA-seq data from melanoma patients from the pre-ICI cohort. First, a signature matrix was generated by using scRNA-seq data from Tirosh *et al.* [7] representing melanoma, CAF, TAM, and $CD8^+$ T cells. Then CIBERSORTx algorithm was used to estimate the cell fractions per bulk RNA-seq sample. To test the significance of cell fractions between Responder and Non-Responder patients of the pre-ICI cohort, the Wilcox test was used. An adjusted p-value < 0.05 was considered significant.

Survival analysis with Kaplan-Meier curve, univariate and multivariate Cox regression analysis

To investigate the impact of LA-TAM on the survival of melanoma patients from the pre-ICI cohort, we first stratify the patients based on the estimated LA-TAM fraction. The patients with higher LA-TAM (top quantile) and lower IFN-TAM (bottom quantile) fractions were considered as $LA\text{-}TAM^{High}$. Similarly, patients with high IFN-TAM (top quantile) and low LA-TAM (bottom quantile) fractions were classified as $IFN\text{-}TAM^{High}$. The remaining patients were classified as Mixed-TAM. A Kaplan-Meier analysis was performed among the three stratified groups. We then performed Cox regression on the tumor samples from the pre-ICI cohort. Confounding factors such as the cohort and therapy categories were also considered. Firstly, a univariate Cox regression analysis followed by a multivariate regression analysis using the survminer R package (https://rpkgs.datanovia.com/survminer/index.html).

Utilization of XGBoost classifier to predict response outcomes

To assess the predictive value of inferred cellular fractions, we implemented a supervised machine learning classifier using Extreme Gradient Boosting (XGBoost) [34]. Estimated fractions of tumor-associated macrophage (TAM) states, $CD8^+$ T cell states, and melanoma cell states were used as input features, while patient response to immune checkpoint inhibition (ICI) served as the outcome variable. Model performance was evaluated independently across six melanoma cohorts using a Leave-One-Out Cross-Validation strategy, in which each cohort was iteratively held out as a test instance while the model was trained on the remaining cohorts. Hyperparameters were tuned with 10 repeats, 5-fold cross-validation during training. Predictive performance was optimized on the area under the receiver operating characteristic curve (AUC). The final model was trained with the best set of hyperparameters on the whole training set (i.e. the remaining 5 cohorts). Feature importance was assessed using the gain metric implemented in the XGBoost framework, enabling identification of the most informative features contributing to response prediction.

Results

TMEs of Non-Responder melanoma patients are characterized by the enrichment of lipid-associated TAMs (LA-TAMs)

To examine TAM heterogeneity in the melanoma TME, we analyzed a $CD45^+$ scRNA-seq dataset (N = 16,291) from 32 patients with known ICI outcomes[4] (Fig. 1A). Following subsetting of macrophages (N = 1,377), Louvain clustering resolved into nine macrophage-subpopulations (C0–C8) (Fig. 1B). Cluster-2 (C2) was marked by high expression of APOE and TREM2 (Additional file 1: Additional file 1: Fig. S1A, Additional file 2: Table S1). Given the prior association between TREM2 + macrophages and ICI resistance [35], we hypothesized that C2 might represent an important macrophage subset that influences the ICI response.

To characterize the macrophage states, we performed UCell enrichment [36] using M2- and M1-macrophage gene signatures [37]. While C2 exhibited the highest M2 enrichment, the difference across clusters was not significant (Fig. 1C), indicating that the conventional M1/M2 classification may not fully recapitulate the heterogeneity observed at single-cell resolution. To better characterize TAM subpopulations, we applied UCell enrichment with seven TAM state gene signatures, including Lipid-associated TAM (LA-TAM) and Interferon-primed TAM (IFN-TAM) [15, 38] (Additional file 2: Table S1). C2 showed significant enrichment for LA-TAM gene signatures (adj $p = 3.2\times10^{-4}$) (Fig. 1D), C4 was enriched for IFN-TAM (adj $p = 1.5\times10^{-3}$) (Fig. 1E), while Inflammatory TAM (Inflam-TAM) signatures were distributed across multiple clusters with the highest enrichment in C3 (Additional file 1: Fig. S1B). To further validate the identity of C2 and C4, we examined key marker genes of LA-TAM and IFN-TAM states. TREM2, APOE, and CD163 exhibited the highest expression in C2 (Fig. 1F, Additional file 1: Fig. S1C), which reinforces the LA-TAM identity of the C2 population. C4 was enriched for IFN-TAM markers CCL2, CCL4, and IFITM1, supporting its classification (Fig. 1F, Additional file 1: Fig. S1D). In contrast, CD68 was uniformly expressed across clusters, reflecting general macrophage identity (Fig. 1F, Additional file 1: Fig. S1D).

We next tested whether LA-TAM enrichment was linked to ICI response. Single-cell enrichment scores were significantly higher in Non-Responders (N = 21) than Responders (N = 11) (adj $p = 1.8\times10^{-11}$) (Fig. 1G, Additional file 2: Table S1), while no other TAM states differed. Longitudinal biopsies were available for 9 out of 32 patients, with pre- and post-treatment (anti-PD1 alone or in combination with anti-CLTA4) time points. Among these longitudinal biopsies (N = 9), LA-TAM enrichment increased post-ICI in Non-Responders (N = 6, adj $p = 2.5\times10^{-12}$) but not in Responders (N = 3) (Fig. 1H, Additional file 2: Table S1). Conversely, IFN-TAM enrichment rose slightly in Responders but declined post-treatment in Non-Responders (adj $p = 4.6\times10^{-4}$) (Fig. 1H, Additional file 2: Table S1), while other TAM states showing no significant changes.

In summary, single-cell analysis revealed that distinct TAM states are linked to a differential outcome of ICI therapy in melanoma patients. The LA-TAM enrichment and IFN-TAM depletion in the TME of Non-

Responders suggested that these TAM states may play opposing roles in determining ICI therapy outcomes.

Lipid metabolic landscape of LA-TAMs in melanoma TME

To explore the lipid metabolic landscape of LA-TAMs, we curated nine gene sets representing distinct lipid-metabolic processes by combining multiple gene set repositories, including REACTOME, KEGG, and GOBP (Additional file 3: Table S2). Enrichment analysis of the macrophage population derived from melanoma TME revealed that the C2 cluster (LA-TAMs) was highly enriched in lipid uptake, cholesterol metabolism, and lipolysis (Fig. 2A and Additional file 1: Fig. S2A), followed by fatty acid oxidation (Additional file 1: Fig. S2A-B). At the gene level, C2 (annotated as LA-TAM) expressed high levels of lipid uptake receptors (CD36, MSR1), cholesterol metabolism regulators (HMGCR, ACAT1/2, ABCA1, ABCG1, NPC1/2), and lipolytic enzymes (LPL, LIPA) (Fig. 2B). Notably, two lipid metabolic pathways (lipid uptake and cholesterol metabolism) were significantly upregulated in Non-Responders compared with Responders (Additional file 1: Fig. S2C). However, enrichment scores did not differ significantly between pre- and post-ICI samples in either group (Additional file 1: Fig. S2D-E).

To compare tumor-resident LA-TAMs with canonical adipose tissue-derived lipid-associated macrophages (LAMs), we integrated scRNA-seq data from melanoma TME-derived TAMs with a curated scRNA-seq dataset from subcutaneous adipose tissue, including Adipose-macrophage cluster-2 (AM2) population defined as LAMs [39]. Integration mapped the adipose-derived macrophages (AM) alongside melanoma TAM clusters (C0-C8), including C2 (LA-TAM) (Fig. 2C). Differential expression and pathway enrichment analysis showed that general fatty acid metabolism, including synthesis and catabolism, was higher in LAMs, whereas LA-TAMs were enriched for specific processes such as phospholipase D signaling, fatty acid β-oxidation, pyruvate metabolism, and glycolysis (Fig. 2D).

To examine the transcriptional concordance between macrophage populations derived from subcutenous adipose tissue and melanoma-TME, we performed correlation analysis confirming that LAMs (AM2) macrophages were most transcriptionally similar to LA-TAMs (C2) (Fig. 2E). Both populations showed high enrichment of lipid uptake and lipolysis (Fig. 2F). Glycolysis and fatty acid oxidation were more strongly enriched in TME-derived LA-TAM compared to adipose tissue-derived LAM, consistent with metabolic adaptation to the hypoxic TME (Fig. 2F). While glycolysis was also detectable in LAM, its pronounced upregulation in LA-TAM suggests a tumor-context–specific amplification of this metabolic program. Increased glycolytic activity in LA-TAM may therefore reflect a broader feature of tumor-resident macrophages adapting to the oxygen-deprived microenvironment.

Together, these results suggest that LA-TAMs acquire an altered lipid metabolic program that partially overlaps with adipose tissue-derived LAMs. Both populations share enhanced lipid uptake, cholesterol metabolism, and lipolysis. However, tumor-resident LA-TAMs also upregulate glycolysis and pyruvate metabolism, reflecting the selective metabolic pressures of the tumor microenvironment.

Spatial continuum of TAM neighborhoods shapes ICI response and relapse

To investigate the localization and potential roles of TAM states within the TME, we compared the spatial organization of TAMs relative to immune and malignant cells between melanoma patients who responded or did not respond to ICI therapy. Briefly, Spatial transcriptomics (stRNA-seq) was performed on FFPE tissue sections retrospectively collected from six melanoma patients (herein referred to as the "UKF" cohort), including three Non-Responders (one primary tumor, one subcutaneous metastasis, and one lymph node metastasis) and three Responders (all subcutaneous metastases) (Additional file 4: Table S3). All biopsies included in this cohort were obtained within 3 months before initiation of ICI treatment. FFPE sections were processed using the Visium Spatial Gene Expression platform (Additional file 4: Table S3), and downstream stRNA-seq analysis was carried out with the SPATA 2.0 package (V3.0.0) [19].

Histological examination of tissue sections by H&E staining (Additional file 1: Fig. S3A), together with BayesSpace clustering of stRNA-seq data, revealed the spatial architecture of the tumor tissues (Fig. 3A-B, Additional file 1: Fig. S3B). In UKF#2, MITF expression marked tumor-enriched regions, mainly in Clusters 4 and 5 (Fig. 3C). Among Responders, MLANA expression in UKF#4 identified C7 as the tumor-enriched region (Fig. 3D). Consistent with these observations, additional marker-based annotation across samples further delineated tumor regions. For instance, in Responders, expression of MLANA (UKF#1) and S100B (UKF#3) defined the tumor regions, with MLANA distributed across C1, C3, C5, and C8 in UKF#1, and S100B confined in C1 and C4 in UKF#3 (Additional file 1: Fig. S3C-D). Similarly, S100B was broadly distributed across C1, C6, C7, and C9 in UKF#5, but confined to C2 in UKF#6 (Additional file 1: Fig. S3E–F). Collectively, the heterogeneous distribution of melanoma markers (MITF, MLANA, S100B) across clusters reflected patient-specific tumor architecture. Differential expression analysis further revealed cluster-specific marker genes that defined distinct immune compositions within spatial neighborhoods (Additional file 4: Table S3). Notably, LA-TAM markers (CD63, MMP1, MMP9, and TREM2) were enriched in C5 of Non-Responders (UKF#1–3) (Additional file 1: Fig. S3G), while IFN-TAM markers (CCL7, CCL2) were localized to C5, C10, and C6 in Responders (UKF#4–6) (Additional file 1: Fig. S3H).

To further resolve cellular architecture, stRNA-seq data were deconvoluted with CytoSPACE [40], mapping major cell types (macrophages, melanoma cells, fibroblasts, $CD8^+$ T cells, $CD4^+$ T cells, B cells, and endothelial cells) onto spatial coordinates using the reference scRNA-seq dataset from Tirosh *et al.* [7]. Based on the cellular composition of spatial clusters, we identified regions with the highest macrophage density and designated them as myeloid-enriched regions. Such regions were observed in C5 of both UKF#2 and UKF#4 (Fig. 3E-F, dashed line), as well as in additional tissue samples (Additional file 1: Fig. S4A, dashed line). Although macrophages represented only ~ 5% of the total tissue (Additional file 1: Fig. S4B), their proportion increased to 22% within myeloid-enriched regions (Fig. 3G, Additional file 4: Table S3). $CD8^+$ T cells constituted 17% of the immune compartment in these regions (Fig. 3G,

Additional file 4: Table S3), making them the second most abundant population and underscoring the potential role of myeloid–T cell neighborhoods in shaping local immune dynamics.

Spatial GSEA was performed to assess TAM states (LA-TAM, IFN-TAM) and T cell subsets (Exhausted-, Activated-, and Memory-effector $CD8^+$ T cells) as reported by Sade-Feldman *et al.* [4] within myeloid-enriched regions (Additional file 4: Table S3). Among Non-Responders, UKF#2 displayed strong LA-TAM enrichment colocalized with Exhausted-CD8 T cells (Fig. 3H). Similar LA-TAM enrichment was observed in UKF#1 and UKF#3 (Additional file 1: Fig. S4C-D), with varying colocalization of Exhausted-CD8 T cells. In UKF#1, Exhausted-CD8 T cells were more diffusely distributed across the tissue (Additional file 1: Fig. S4C), while in UKF#3, Exhausted-CD8 T cells occupied an adjacent niche in Cluster 4, separate from the LA-TAM-enriched region (Additional file 1: Fig. S4D). In Responders, UKF#4 showed predominant IFN-TAM enrichment within the myeloid-enriched region, accompanied by partial overlap with Activated-CD8 T cells, while weak LA-TAM and Exhausted-CD8 signals were localized outside this region (Fig. 3I). Consistently, UKF#5 and UKF#6 exhibited IFN-TAM and Activated-CD8 colocalization in myeloid-enriched regions (Additional file 1: Fig. S4E-F). Notably, UKF#6 also contained spatially distinct LA-TAM and Exhausted-CD8 niches, mirroring the pattern in UKF#4 (Additional file 1: Fig. S5F). In Non-Responders, colocalization of LA-TAM and Exhausted-CD8 was further supported by overlapping APOE, TREM2, and TIM3 (HAVCR2) expression in UKF#2 and UKF#3 within myeloid-enriched regions (Additional file 1: Fig. S5A). In contrast, the Responder UKF#4 exhibit colocalization of IFN-TAM markers (CCL2, CCL4) with Granzyme B, indicative of an immunostimulatory microenvironment (Additional file 1: Fig. S5B). Notably, APOE and TREM2 expression in UKF#4 and UKF#6 indicated the presence of LA-TAMs in Responders as well, albeit confined in spatially distinct niches (Additional file 1: Fig. S5B).

The coexistence of different TAM and $CD8^+$ T cell states in overlapping, partially overlapping, and non-overlapping regions implies the need to quantify the diverse cellular localization within functional spatial-neighborhoods across the tissue sections. To address this, a spatial neighborhood analysis with a 250 μm radius as a functional interaction region [41] was used to quantify colocalization of TAMs and T cell states with melanoma states defined by Tsoi *et al.* [16] (Additional file 4: Table S3). Across the three Non-Responders, a conserved neighborhood comprising LA-TAM, Exhausted-CD8 T cells, and Neural Crest-like melanoma was consistently observed (Fig. 3J). In the three Responders, neighborhoods were enriched for IFN-TAM, Activated-CD8, and Memory-effector T cells, while LA-TAM and Neural Crest-like melanoma also colocalized in spatially distinct regions (Fig. 3K). Analysis of individual samples revealed sample-specific heterogeneity. In UKF#3 (Non-Responder), IFN-TAM colocalized with Activated-CD8 T cells despite the overall non-responsive phenotype, while LA-TAM and Exhausted-CD8 cells occupied a separate niche (Additional file 1: Fig. S5C). Similarly, in UKF#4 (Responder), LA-TAM also coexisted with Exhausted-CD8 T cells. This indicates that immunosuppressive niches persist alongside IFN-TAM and Activated-CD8 neighborhoods even in clinically responsive tumors (Additional file 1: Fig. S5D). These findings suggest that even among Responder patients, enriched for IFN-TAM and Activated-CD8 T cells, LA-TAM and Exhausted-CD8 T cells persist in discrete tumor regions, potentially maintaining localized immunosuppression within an otherwise immune-active environment.

The coexistence of functionally opposing TAM neighborhoods within the same tumor sample prompted us to examine their association with ICI therapy outcomes. We calculated patient-level LA-TAM (LA-TAM with Exhausted-CD8 T cells and Neural Crest-like melanoma) and IFN-TAM (IFN-TAM with Activated- and Memory-effector CD8 T cells) neighborhood scores based on colocalization. As expected, Non-Responders showed high LA-TAM but low IFN-TAM neighborhood scores, whereas Responders exhibited the opposite pattern (Fig. 3L). Notably, UKF#3 and UKF#4 displayed comparably higher scores for both neighborhoods before therapy initiation. Although UKF#4 was initially classified as a Responder based on a partial response (PR) during the first months of ICI treatment, progressive disease (PD) was observed at a second follow-up, which may be explained by the presence of LA-TAM neighborhoods contributing to relapse.

In summary, spatial-transcriptomics analysis revealed the coexistence of functionally opposing TAM neighborhoods within individual melanoma lesions, highlighting their prognostic relevance for ICI therapy. Non-Responders were characterized by dominant LA-TAM neighborhoods enriched with Exhausted-CD8$^+$ T cells and Neural Crest-like melanoma regions, whereas Responders displayed IFN-TAM and Activated-/Memory-CD8$^+$ neighborhoods consistent with immune activation. Importantly, the coexistence of both neighborhood types within the same tumor, as observed in patient UKF#4, coincided with disease relapse despite an initial response, suggesting that persistent LA-TAM–driven immunosuppressive niches may compromise durable therapeutic benefit.

These findings underscore that TMEs exist along a continuum defined by the relative dominance of LA-TAM and IFN-TAM neighborhoods, which acts as a critical determinant of ICI treatment outcome. A similar principle, albeit in the opposite direction, was observed in UKF#3. This patient exhibited a high LA-TAM fraction but also a comparatively elevated IFN-TAM component relative to UKF#1 and UKF#2. Notably, UKF#3 transitioned from initial progressive disease (PD) to stable disease (SD), suggesting that a relatively increased presence of IFN-TAM neighborhood may partially counterbalance LA-TAM–associated immunosuppression for this particular patient.

TGF-β signaling is dominant in the LA-TAM neighborhood in Non-Responder patients

Having defined LA-TAM and IFN-TAM neighborhoods, we next compared upregulated pathways within these neighborhoods across Responder and Non-Responder patients. In Non-Responders, LA-TAM neighborhoods were consistently enriched for TGF-β signaling, as reflected by TGFB-receptor signaling and downstream SMAD activation, which emerged as the only pathway upregulated across all Responder patients (Fig. 4A, Additional file 5: Table S4). A hypoxia response signature was additionally upregulated in two patients (UKF#2 and UKF#3). Other pathways, such as cholesterol biosynthesis, ECM organization, and IL-10 signaling, showed patient-specific enrichment, being upregulated in only one of the three Non-Responders. To dissect the TGF-β signaling network within LA-TAM neighborhoods, we examined the individual genes contributing to its activation. This analysis revealed upregulation of key signaling components, including the ligand (TGFB1), receptors (TGFBR1 and TGFBR2), downstream

mediators (SMAD2 and SMAD4), and target genes such as LOXL2 (Fig. 4B, Additional file 5: Table S4). Notably, the concomitant presence of TREM2, a canonical LA-TAM marker, suggests that TGF-β signaling may contribute to the regulation of TREM2 expression within these neighborhoods (Fig. 4B). In UKF#2, spatial mapping showed that TGF-β signaling components, including the TGFB1, TGFBR1, and SMAD2/4, were highly expressed within the LA-TAM neighborhood (Fig. 4C).

In contrast, IFN-TAM neighborhoods showed upregulation of interferon-related pathways (Type I IFN production and IFN-α/β signaling) together with T cell activation (α/β T cell activation) across all three Responder patients (Fig. 4D, Additional file 5: Table S4). Within these regions, canonical IFN-TAM markers such as CCL2, IFITM1, HLA-A, and IRF7 were highly expressed (Fig. 4E, Additional file 5: Table S4). Interestingly, TFRC (CD71), a component of the IFN-signaling network, was also upregulated (Fig. 4E), suggesting that IFN signaling may induce TFRC expression in IFN-TAM neighborhoods, thereby contributing to T cell activation. Spatial mapping of IFITM1, HLA-A, and TFRC revealed expression not only within IFN-TAM neighborhoods but also in adjacent regions, indicating partial overlap with neighboring cellular niches (Fig. 4F).

Given that TGF-β signaling emerged as the dominant immunosuppressive pathway in LA-TAM neighborhoods of Non-Responders, we next investigated the initiating and receiving cell types engaged via TGF-β signaling. Spots enriched for the dominant cell types in LA-TAM neighborhood (i.e., LA-TAM, Exhausted-CD8 T cells, and Neural Crest-like melanoma (NCL) were identified in Non-Responder samples (UKF#2 is shown as a representative case, Fig. 4G). CellChat analysis of the identified spots across three samples revealed that the implicated cell types could serve both as senders and receivers of TGF-β signaling (Fig. 4H). The strongest signaling probability was observed in the reciprocal interaction between LA-TAM and NCL cells, with LA-TAM also displaying prominent autocrine TGF-β signaling (Fig. 4H). In addition, APOE–TREM2 signaling was detected, predominantly mediated from NCL to LA-TAM (Fig. 4H).

In Responders, we next identified spots enriched for dominant IFN-TAM neighborhood signatures (i.e., IFN-TAM, Activated-CD8 T cells, and Memory-effector T cells), with UKF#4 shown as a representative case (Fig. 4I). Cell-cell communication analysis highlighted CCL and HLA signaling as the major pathways (Fig. 4J). CCL signaling originated from Activated-CD8 and Memory-effector T cells, with IFN-TAM serving as the primary recipient. Conversely, IFN-TAM mediated HLA-based interactions directed toward both Activated-CD8 and Memory-effector T cells (Fig. 4J).

Our findings highlight the interplay between LA-TAMs, exhausted-CD8, and malignant cells in shaping the immunosuppressive TME of metastatic melanoma. Cell-cell communication analysis identified TGF-β and APOE–TREM2, as key signaling pathways reinforcing this crosstalk. LA-TAMs emerged as central hubs, acting as both senders and receivers of these signals. These insights suggest potential therapeutic strategies targeting these signaling networks to restore anti-tumor immunity.

Spatially confined lipid metabolic pathways define LA-TAM–dominated niches

While our single-cell transcriptional analyses highlighted the lipid metabolic reprogramming in LA-TAMs, spatial analysis is essential to determine whether the lipid-metabolic programs align with LA-TAM–centric immunosuppressive niches. This spatial context is critical to link metabolic specialization with LA-TAM function and clinical outcome.

To investigate the spatial organization of lipid metabolic pathways, we first examined pathway enrichment in LA-TAM regions of the Non-Responder sample UKF#2 as a representative case. Lipid metabolic pathways, including lipid uptake, fatty acid (FA) oxidation, FA synthesis, and cholesterol metabolism, were highly enriched in the LA-TAM neighborhood (Fig. 5A), suggesting that the dominant LA-TAM population locally upregulates these pathways.

To systematically assess these patterns, we compared the spatial distribution of lipid metabolic pathways across LA-TAM, IFN-TAM, and adjacent tumor regions in both Non-Responder and Responder samples. Lipid uptake, FA oxidation, and cholesterol metabolism were markedly enriched in Non-Responders compared with Responders (Fig. 5B, Additional file 6: Table S5). In Non-Responder samples UKF#1 and UKF#2, LA-TAM regions showed strong enrichment of lipid uptake, oxidative phosphorylation, and cholesterol metabolism. LA-TAM regions in UKF#2 and UKF#3 also displayed elevated FA oxidation and glycolysis (Fig. 5B). Notably, glycolysis was spatially colocalized between LA-TAM and neighboring tumor regions, with both compartments enriched for glycolytic activity in Non-Responders (Fig. 5B). FA synthesis was largely confined to tumor regions of Non-Responders, whereas Responder TMEs were broadly devoid of FA synthesis activity (Fig. 5B). Although some tumor regions in Responders showed limited lipid pathway enrichment, IFN-TAM regions were mostly devoid of lipid metabolic activity, apart from oxidative phosphorylation and ROS production observed in UKF#4 (Fig. 5B). Interestingly, patient UKF#4, who initially responded but later relapsed, exhibited relatively higher enrichment of ROS production, oxidative phosphorylation, and cholesterol metabolism compared with other Responder samples (Fig. 5B).

To quantify differences in lipid metabolic activity between the TAM neighborhoods and adjacent tumor regions across Non-Responder and Responder samples, we compared the distribution of enrichment scores of spatial spots localized within LA-TAM, IFN-TAM, and corresponding adjacent tumor regions. Among the analyzed pathways, Lipid Uptake, Lipolysis, and Cholesterol Metabolism displayed the most pronounced difference between LA-TAMs and the adjacent tumor region across Non-Responders (Fig. 5C, Additional file 6: Table S5), indicating a marked upregulation of lipid metabolic processes confined to LA-TAM neighborhoods. In contrast, ROS production was significantly higher in IFN-TAM compared to the adjacent Tumor regions across the Responder patients (Fig. 5C, Additional file 6: Table S5).

To further investigate gene-level regulation, we calculated the fold change of genes associated with Lipid Uptake, Lipolysis, and Cholesterol Metabolism between LA-TAM and adjacent tumor regions, as well as between IFN-TAM and adjacent tumor regions (Fig. 5D). This analysis revealed that lipid-metabolism related genes were predominantly upregulated in LA-TAMs relative to their adjacent tumor regions,

whereas these genes were downregulated in IFN-TAMs compared to neighboring tumor regions (Fig. 5D).

Collectively, these findings indicate that lipid metabolic reprogramming in ICI Non-Responders is primarily confined to LA-TAM–dominated neighborhoods rather than the tumor compartment itself. The spatial localization of lipid uptake pathway within LA-TAM regions underscores their potential role as localized hubs of metabolic adaptation within the Non-Responder TME.

Spatial proteome profiling reveals an immune exclusion–activation continuum in melanoma TME

Building on the stRNA-seq findings, we further analyzed the immune microenvironment at the protein level using spatial proteome profiling with imaging mass cytometry (IMC) (Antibody panels used in IMC are reported in Additional file 7: Table S6). IMC was performed on tissue sections from the UKF cohort. This approach enabled high-resolution characterization of immune and tumor cell localization, providing insights into the spatial distribution and protein expression patterns that shape the tumor microenvironment and influence therapeutic outcomes.

The cellular composition was determined after segmentation and phenograph clustering. 14 cell types were identified, reflecting distinct tumor, immune, and stromal cell populations (Fig. 6A, Additional file 1: Fig. S6A). Immune cell populations, including T cells (expressing CD8a, CD3, and CD45) and myeloid cells (expressing CD14, CD68, CD204, and CD163), were identified showing differential expression of key immune markers. In addition, stromal compartments consisting of Cancer-associated fibroblast (CAF: Collagen1), Perivascular CAF (Peri-CAF: Collagen1, CD34), and Stroma (SMA) were identified. Melanoma cells were annotated based on the expression of the S100 marker. UMAP visualization of single-cell IMC data (Fig. 6B) demonstrated the separation of major immune, stromal, and tumor cell populations, with clear distinctions between $CD8^+$ T cells and myeloid cells.

Further sub-clustering of the myeloid compartment (Fig. 6C-D, and Additional file 1: Fig. S6B) identified distinct subpopulations, including LA-TAM and IFN-TAM states. LA-TAM subpopulation was identified based on the high expression of canonical LA-TAM markers, including TREM2, APOE, and CD163 (Fig. 6C). In contrast, IFN-TAMs were annotated based on the expression of CCL2, CCL4, and CD68 (Fig. 6C). A comparison of myeloid subset distribution showed significant enrichment of IFN-TAM and Antigen-presenting Macrophage 1 (AMP1) states in ICI Responders compared to Non-Responders ($P = 0.0039$) (Fig. 6E). Similarly, the $CD8^+$ T cell compartment defined by the high expression of CD8a was analyzed (Fig. 6F-G), where distinct subsets were identified, including $TIM3^+$ $CD8^+$ T cells and granzymeB $(GZMB)^+$ cytotoxic $CD8^+$ T cells. The proportional abundance of these $CD8^+$ T cell subsets differed significantly between Responders and Non-Responders (Fig. 6H), with Responders displaying a higher fraction of $GZMB^+$ $CD8^+$ T cells ($P = 0.024$).

Neighborhood-centric intercellular interaction analysis was performed by aggregating all annotated cells across the three Responders and three Non-Responders tissue samples. This combined analysis revealed distinct spatial organization patterns of LA-TAM and IFN-TAM populations between Non-Responder and Responder groups. Heatmaps of interaction signal strength (Fig. 6I–J), representing data pooled from all samples within each group, showed a stronger interaction signal between $TIM3^+$ $CD8^+$ T cells and LA-TAMs in Non-Responders (UKF#1, UKF#2, and UKF#3). In contrast, Responders (UKF#4, UKF#5, and UKF#6) exhibited higher interaction signals between $GZMB^+$ $CD8^+$ T cells and IFN-TAMs, suggesting a more effective anti-tumor immune response. Additionally, a weaker interaction between $TIM3^+$ $CD8^+$ T cells and LA-TAMs was also observed in Responders.

Representative IMC images highlight pronounced differences in the spatial architecture and cellular composition of the tumor microenvironment (TME) between Non-Responder (UKF#2) and Responder (UKF#4) patients (Fig. 6K–L). The Non-Responder TME exhibited a deserted architecture, with sparse $CD8^+$ T cell infiltration and strong enrichment of $APOE^+TREM2^+$ LA-TAMs, which were spatially localized in proximity to sparsely distributed $TIM3^+$ exhausted $CD8^+$ T cells (Fig. 6K). This organization suggests that LA-TAM–dominated niches may restrict the recruitment and activation of cytotoxic T cells, contributing to an immunosuppressive and exclusionary microenvironment. In contrast, the Responder TME displayed pronounced immune infiltration with an immune-active landscape, characterized by abundant $GZMB^+$ $CD8^+$ T cells intermingled with $CCL4^+$ IFN-TAMs (Fig. 6L), indicative of a cytotoxic response. Interestingly, LA-TAMs and $TIM3^+$ $CD8^+$ T cells were also detectable in Responder tissue (Fig. 6L), further reinforcing the coexistence of functionally opposing TAM neighborhoods within the same tumor, consistent with observations from the spatial transcriptomic analysis.

In summary, spatial IMC profiling provides protein-level, cross-platform validation of the distinct immune architectures identified by spatial transcriptomics, confirming both their spatial organization and differential abundance across ICI Responders and Non-Responders. Non-Responders exhibited a TME characterized by strongly colocalized immunosuppressive $APOE^+TREM2^+$ LA-TAMs and sparsely distributed exhausted $TIM3^+$ $CD8^+$ T cells, consistent with an immune-excluded phenotype devoid of cytotoxic $CD8^+$ T cells. In contrast, Responders displayed an immune-active microenvironment with enriched $CCL4^+$ IFN-TAMs and colocalized $GZMB^+$ cytotoxic $CD8^+$ T cells, reflecting enhanced anti-tumor immunity. Importantly, the coexistence of these opposing spatial niches across samples further supports the presence of a continuum between immune exclusion and immune activation, defined by the relative dominance of LA-TAM and IFN-TAM neighborhoods. Together, these findings provide proteome-level evidence that both the spatial arrangement and abundance of TAM-associated immune niches critically shape ICI response in metastatic melanoma.

Analysis of a large melanoma cohort reveals TAM states as robust predictors of immunotherapy outcome

To validate the association between TAM states and resistance to ICI therapy, we assembled a large pre-treatment bulk RNA-seq cohort comprising 334 melanoma patients from six independent studies (Hugo

et al. [27], Riaz *et al.* [28], Van-Allen *et al.* [29], Liu *et al.* [30], Gide *et al.* [31], MGH [32]) referred to herein as "pre-ICI Cohort" (Fig. 7A). Importantly, all samples were obtained prior to ICI initiation, enabling assessment of predictive biomarkers for ICI therapy outcomes. The majority of patients received anti-PD-1/PD-L1 monotherapy, with smaller subsets treated with anti-CTLA-4 or combination regimens (Fig. 7A).

To interrogate TME composition from bulk transcriptomics, we utilized CIBERSORTx [37] to construct a signature matrix (Additional file 8: Table S7) from single-cell data [7] encompassing major melanoma (Melanocytic, Transitory, NCL), TAM (LA-TAM and IFN-TAM), and $CD8^+$ T cell (activated and exhausted) states (Fig. 7B). These signatures were subsequently projected onto the pre-ICI bulk cohort to quantify cell-type fractions (Additional file 8: Table S7).

Next, we compared the fractions of major cell types (Melanoma, TAM, CAF, and $CD8^+$ T cells) between Non-Responders (N = 196) and Responders (N = 138) (Fig. 7C). Consistent with prior observations, Responders exhibited significantly higher $CD8^+$ T cell fraction, whereas Non-Responders displayed a more $CD8^+$ T cell-depleted microenvironment (Fig. 7C). Further comparison of melanoma states did not exhibit a significant difference (Fig. 7D). However, we observed distinct TAMs and $CD8^+$ T cell states associated with differential response outcomes. For instance, LA-TAMs were significantly enriched in Non-Responders (Fig. 7E), while IFN-TAMs (Fig. 7E) and activated $CD8^+$ T cells (Fig. 7F) were significantly increased in Responders. These results reinforce the concept that TAM states are tightly linked to T cell functionality and therapeutic response.

To assess clinical relevance, patients were stratified based on LA-TAM and IFN-TAM fractions. LA-TAM^{high} patients were defined by high LA-TAM (top quantile) and low IFN-TAM (bottom quantile), whereas IFN-TAM^{high} patients showed the opposite pattern. Patients exhibiting intermediate or concurrent levels of both TAM states were classified as Mixed-TAM.

LA-TAM^{high} patients exhibited significantly worse overall survival, whereas IFN-TAM^{high} patients showed improved outcomes (Fig. 7G). Notably, patients with Mixed-TAM profiles had survival outcomes comparable to the LA-TAM^{high} group, indicating that the presence of LA-TAMs is sufficient to override the beneficial effects of IFN-TAMs (Fig. 7G). This highlights a dominant, immunosuppressive role for LA-TAMs within the TME. Univariate- and Multivariate- Cox regression analysis further supported these findings (Additional file 8: Table S7), where higher LA-TAM fractions were independently associated with poor survival (HR: 1.23, FDR: 0.003), while IFN-TAMs were associated with favorable outcomes (HR: 0.59, FDR: 0.00001), after adjusting for cohort and therapy effects (Additional file 1: Fig. S7A-B). Together, these results establish TAM state composition as an independent determinant of patient prognosis.

Building on our deep spatial profiling, we estimated the fraction of TAM-centered cellular neighborhoods. By combining fractions of LA-TAMs, Neural crest-like melanoma, and exhausted $CD8^+$ T cells, we defined an LA-TAM neighborhood, while the combined fractions of IFN-TAMs and activated-CD8 T cells

represented an IFN-TAM neighborhood. Next, we compared the TAM-neighborhood across patients stratified by detailed response categories (Progressive disease: PD, Stable disease: SD, Partial response: PR, and Complete Response: CR). Our results uncovered that patients were distributed along a continuum between these opposing neighborhood states (Fig. 7H). PD (N = 114) and SD (N = 31) patients were strongly enriched for LA-TAM neighborhood states, whereas CR patients (N = 24) exhibited a higher fraction of IFN-TAM neighborhoods (Fig. 7H). Importantly, even PR patients (N = 54) retained substantial fractions of the LA-TAM neighborhood (Fig. 7H), suggesting that the persistence of this immunosuppressive neighborhood may limit full therapeutic efficacy to CR. As observed earlier, patients who initially exhibited PR could subsequently progress to PD or SD at the second follow-up (Fig. 3L). The presence of a substantial LA-TAM fraction in the PR patients may contribute to this relapse (Fig. 7H).

To assess whether the cellular fractions derived from the bulk RNA-seq data can predict patient response outcomes prior to ICI initiation, we employed a machine learning-based XGBoost classifier model [34]. Model performance was systematically evaluated across the six independent cohorts using a Leave-One-Out-Cross-Validation approach. The results demonstrated that the estimated cellular fractions of TAM, $CD8^+$ T cells, and melanoma states can reliably predict patient response outcomes, with AUCs ranking from 0.764 (MGH cohort) to 0.946 (Riaz *et al.)* (Fig. 7I and S7C). Feature importance analysis revealed that the LA-TAM fraction was the most informative predictor of response outcome, followed by the Activated-$CD8^+$ T cell fraction (Fig. 7J).

Taken together, these findings demonstrate that TAM states, particularly the abundance of LA-TAMs, serve as robust pre-treatment predictors of both ICI response and patient survival. Importantly, our study provides a clinically translatable framework by introducing a single-cell-derived signature matrix of the melanoma TME. This approach enables the decomposition of any bulk transcriptomic data from melanoma patients into functionally relevant components, including LA-TAM fractions, thereby facilitating the prediction of ICI response prior to treatment.

Discussion

Through integrative bulk, single-cell, and spatial multi-omics profiling, we delineated the immune architecture of the infiltrative region of melanoma tumors and identified key determinants of ICI resistance and response. Non-Responder TMEs were characterized by immunosuppressive LA-TAM neighborhoods enriched for LA-TAMs colocalizing with Exhausted-$CD8^+$ T cells and NCL melanoma, whereas Responder TMEs exhibited IFN-TAM neighborhoods spatially associated with Activated- and Memory-$CD8^+$ T cells, indicative of an immune-active milieu.

Lipid-associated macrophages (LAMs) have been extensively characterized in metabolic diseases such as obesity and atherosclerosis, where they arise from circulating monocytes under the control of TREM2 and acquire a conserved lipid-handling signature marked by APOE, C1QB, CD9, and CD36 expression [14]. These cells are thought to mediate lipid clearance and tissue remodeling in response to metabolic stress. However, whether a functionally analogous TAM population exists within the tumor

microenvironment (TME) has remained unexplored. In particular, no prior studies have systematically compared adipose tissue-derived LAMs with tumor-resident lipid-associated TAMs (LA-TAMs) that emerge under oncogenic and immune pressures. Our comparative single-cell and spatial analyses address this gap by demonstrating that melanoma TME-derived LA-TAMs share core lipid metabolic programs with LAMs, yet exhibit distinct adaptations reflecting the unique metabolic constraints of the hypoxic tumor niche (Fig. 2F). Our results uncovered that TME-resident LA-TAMs adopt a distinct lipid metabolic phenotype characterized by enhanced lipid uptake, cholesterol metabolism, lipolysis, and fatty acid oxidation, alongside increased glycolytic activity (Fig. 2F and 5B). This metabolic configuration partially overlaps with that of adipose tissue-derived LAMs described in obesity and atherosclerosis, which similarly rely on lipid scavenging through CD36 and TREM2–APOE signaling pathways [39, 42]. However, unlike adipose LAMs, LA-TAMs within the melanoma TME displayed upregulation of glycolytic and β-oxidation programs, likely reflecting adaptation to hypoxic and nutrient-restricted tumor niches [43].

Given that LA-TAMs exhibit altered lipid metabolic profiles, further investigation into whether TME lipid profiles influence ICI response is warranted. Dysregulated lipid metabolism has been linked to immune suppression and TAM polarization [44], raising the possibility that aberrant lipid metabolism could shape the TME and modulate immunotherapy efficacy. Future studies examining circulating lipid levels, TME lipid composition, and lipid metabolic pathways in Responders and Non-Responders may uncover metabolic vulnerabilities that could be targeted to enhance ICI response. Consistent with this notion, recent work has shown that the anti-anginal drug ranolazine can sensitize BRAFi-resistant melanoma to immunotherapy by targeting fatty acid oxidation, highlighting lipid metabolism as a promising therapeutic axis [45].

Aided by the spatial neighborhood analysis, the presence of LA-TAM neighborhoods emerged as the dominant determinant of patient prognosis, regardless of the coexistence of IFN-TAM regions. Although IFN-TAM-enriched areas were generally associated with a clinical response, the presence of these areas alone did not guarantee a sustained benefit when LA-TAM neighborhoods coexisted within the same tumor. Patients harboring LA-TAM-dominated neighborhoods were consistently classified as Non-Responders at baseline or experienced progressive disease at follow-up, as exemplified by patient UKF#4 (Fig. 3L). These results suggest that LA-TAM-driven immunosuppressive microenvironments can override IFN-TAM-mediated immune activation, ultimately dictating therapeutic failure. Thus, the spatial dominance of LA-TAM neighborhoods may serve as a robust determinant of poor prognosis and limited durability of ICI response in melanoma.

The increased presence of LA-TAMs in Non-Responders suggests their pivotal role in immune evasion, warranting further investigation into their functional interactions within the TME. The co-localization of LA-TAMs with exhausted $CD8^+$ T cells in Non-Responders (Fig. 3J and 6I) suggests potential reciprocal interactions that contribute to immune suppression. Our spatial analysis highlighted the crosstalk between LA-TAMs, exhausted $CD8^+$ T cells, and neural crest-like (NCL) melanoma (Fig. 4G), revealing a coordinated immunosuppressive network that shapes the metastatic melanoma TME. This network,

driven by TGF-β and APOE-TREM2 signaling pathways, underscored the functional role of LA-TAMs as both immunosuppressive signal senders and receivers. Notably, we identified TREM2-expressing LA-TAMs as the exclusive recipient of APOE ligand from neural crest-like melanoma cells, while simultaneously engaging in autocrine APOE-TREM2 signaling (Fig. 4G). This dual paracrine-autocrine APOE-TREM2 signaling loop likely establishes a self-sustaining feed-forward mechanism that amplifies the immunosuppressive role of LA-TAMs in shaping the TME. This aligns with prior studies showing that tumors and CAFs reprogram blood monocytes into LA-TAMs [46] and consequently establish an immunosuppressive niche that impairs T cell-mediated anti-tumor responses [47, 48]. Importantly, APOE-TREM2 signaling has been implicated in immune regulation beyond melanoma, particularly in neurodegenerative diseases, where APOE-expressing myeloid cells suppress inflammatory responses [49]. This suggests a conserved mechanism by which $APOE^+$ LA-TAMs exploit TREM2 to dampen anti-tumor immunity. Furthermore, the communication between LA-TAM, $CD8^+$ T cell, and malignant compartments through TGF-β signaling mirrors observations in other cancers, where these cytokine signaling pathways drive T cell exhaustion and immune escape [50]. Future studies are required to explore combinatorial strategies combining TGF-β /TREM2-targeting therapies with ICIs, as recent evidence indicates that TREM2 inhibition enhances T-cell infiltration and improves responses to ICI therapy [51].

In contrast to this suppressive environment, an anti-tumor immune landscape emerges in Responders, characterized by the spatial proximity of IFN-TAMs and activated $CD8^+$ T cells (Fig. 3K and 6J). Studies have shown that the spatial distribution of immune cells within the TME influences ICI efficacy, with activated $CD8^+$ T cells in proximity to tumor cells correlating with improved outcomes [52]. Type I interferon signaling also plays a key role in this process, as IFN-TAMs enhance cytotoxic T-cell infiltration and promote ICI response [53]. Our findings support this concept by demonstrating that IFN-TAMs spatially coincide with activated $CD8^+$ T cells. Additionally, our stRNA-seq analysis highlights the chemokine and HLA-signaling mediated crosstalk between IFN-TAMs and activated $CD8^+$ T cells (Fig. 4J), providing key insights into how IFN-TAMs shape the immune landscape and influence ICI response in melanoma.

Spatial proteome profiling using imaging mass cytometry (IMC) provided a deeper insights into the comparison of spatial TME organization between Non-Responder and Responder and revealed striking differences in immune cell density and spatial composition of the TME. The Non-Responder TME exhibited an immune-exclusionary architecture, characterized by sparse $CD8^+$ T cell infiltration and a strong enrichment of $APOE^+TREM2^+$ LA-TAMs. The latter were localized in proximity to scattered $TIM3^+$ exhausted $CD8^+$ T cells (Fig. 6K), reinforcing an immunosuppressive niche [47] [54]. This organization suggests that LA-TAM-dominated neighborhoods may restrict the recruitment and activation of cytotoxic T cells. In contrast, the Responder TME displayed an immune-active landscape with dense immune infiltration, marked by abundant $GZMB^+$ $CD8^+$ T cells intermingled with $CCL4^+$ IFN-TAMs (Fig. 6L). This pattern is consistent with a cytotoxic and pro-inflammatory milieu that supports effective anti-tumor immunity and enhances ICI efficacy [55]. Notably, LA-TAMs remained detectable in Responder tumors

(Fig. 6L), suggesting that targeting residual immunosuppressive TAM populations could further improve therapeutic outcomes. The persistence of immunosuppressive LA-TAM neighborhoods, regardless of response status, may explain the limited rates of complete responses to ICI therapy, as well as relapse following an initial response. Indeed, complete remission remains relatively uncommon, with reported rates of approximately 22% for combination ICI therapy (ipilimumab plus nivolumab), 19% for nivolumab monotherapy, and only 6% for ipilimumab alone [56].

Lastly, analysis of bulk transcriptomic data from a large validation cohort of 334 patients confirms that functionally opposing TAM fractions serve as critical determinants of clinical outcomes such as ICI response and survival. The melanoma TME-derived signature-matrix generated in the current study (Additional file 8: Table S7) is readily applicable to independent patient cohorts, including routine bulk RNA-seq datasets, to estimate TAM and $CD8^+$ T cell abundance prior to therapy. Such stratification has immediate clinical utility, enabling the identification of patients at high risk of ICI resistance before treatment initiation. In contrast to earlier macrophage-related signatures, such as the one described by Xiong et al. [13], our signature matrix provides a higher-resolution decomposition of TAM heterogeneity. While the former captures macrophage-associated resistance along a unidirectional axis, our approach resolves a continuum of functionally distinct TAM states by specifically decoupling the immune-active IFN-TAM state from the immunosuppressive LA-TAM state. This higher-resolution stratification enables the identification of patients with mixed-TAM compositions and more accurately captures the underlying complexity of the tumor microenvironment.

Conclusion

In summary, our study defines the cellular, metabolic, and spatial foundations of macrophage heterogeneity in melanoma. We uncover the coexistence of functionally opposing TAM neighborhoods that confine distinct immune states within the tumor microenvironment. LA-TAM neighborhoods exert a dominant immunosuppressive effect that overrides IFN-TAM–associated immune activation and dictates adverse clinical outcomes. Finally, we establish a clinically actionable framework that enables the inference of spatially defined immune composition from bulk transcriptomic data. This approach enables robust estimation of TAM fractions and facilitates pre-treatment patient stratification based on predicted ICI response.

Declarations

Data availability

All publicly available data sets analyzed in this study are cited in the manuscript. The spatial transcriptomics data generated in this study have been deposited in Zenodo (https://zenodo.org/records/14930564) with DOI: 10.5281/zenodo.14930564. Imaging mass cytometry data was deposited in Zenodo with DOI: https://doi.org/10.5281/zenodo.14930564.

All original code used for analysis and generation of Figures is freely available in the GitHub repository at https://github.com/schak-scs/Melanoma_2026.

Acknowledgments

The authors express their gratitude to Christine Gretzmeier for her technical support with tissue section mounting and to the high-throughput sequencing unit team of the DKFZ Genomics and Proteomics Core Facility in Heidelberg for providing the sequencing services.

Research funding

MB is supported by the Deutsche Forschungsgemeinschaft (DFG) – CRC1479 (Project ID 441891347-S1), CRC 1160 (Project ID 256073931-Z02), CRC1453 (Project ID 431984000 – S1), TRR167 (Project ID 259373024-Z01), TRR417 (Project ID: 540805631-TP S03), TRR 353/1 (Project ID 471011418-SP02), FOR 5476 UcarE (Project ID 493802833-P7) and by German Federal Ministry of Education and Research (BMBF), PM4Onco–FKZ 01ZZ2322A, SATURN3 (01KD2206L). GA, SC, TD and CK are supported through MIRACUM consortia funded by the BMBF as part of the Medical Informatics Initiative (EkoEstMed–FKZ 01ZZ2015). NM is supported by funding from DFG: MeInBio: 322977937/GRK2344. The research was supported by other DFG grants: # 520992132, # 441891347 (OncoEscape), # 390939984 (CIBSS), # 272983813 (TRR179), # 256073931 (IMPATH), and # 518316185 (GMCA).

Contributions

SC, GA, and MB conceptualized the manuscript. FM and DR recruited the patients, obtained the clinical data, evaluated the response status of the patients, and collected the tissue samples. AN processed the tissue block. EC and NM performed the H&E staining and the spatial-transcriptomics experiments on the tissue slices. IG and BB performed the imaging mass cytometry experiment. All the data, including publicly available bulk and single-cell RNA-seq as well as in-house generated spatial-transcriptomics and IMC datasets generated in-house, were analyzed by SC, TD, CK, IG, and GA. SC, TD, and CK performed the spatial-neighborhood analysis. SC, EC, GA, and MB wrote the manuscript. All authors read and approved the final manuscript.

Ethics declarations

Consent and ethical approval were obtained from the Local Regional Ethics Commission of University Hospital Freiburg (Ethics Approval Reference: 24-1387-S1). All the participants in the current study provided written informed consent to participate. All the protocols and research conformed to the principles of the Helsinki Declaration.

Declaration of interests

The authors declare no competing interests.

References

1. Hodi FS, O'Day SJ, McDermott DF, Weber RW, Sosman JA, Haanen JB et al. Improved Survival with Ipilimumab in Patients with Metastatic Melanoma. New England Journal of Medicine [Internet]. Massachusetts Medical Society; 2010 [cited 2024 Jun 3];363:711–23. https://doi.org/10.1056/NEJMOA1003466/SUPPL_FILE/NEJMOA1003466_DISCLOSURES.PDF
2. Weber JS, D'Angelo SP, Minor D, Hodi FS, Gutzmer R, Neyns B, et al. Nivolumab versus chemotherapy in patients with advanced melanoma who progressed after anti-CTLA-4 treatment (CheckMate 037): a randomised, controlled, open-label, phase 3 trial. Lancet Oncol Elsevier. 2015;16:375–84. https://doi.org/10.1016/S1470-2045(15)70076-8.
3. Zhang Z, Langenbach M, Sagar S, Fetsch V, Stritzker J, Severa E et al. Efficacy of CTLA-4 checkpoint therapy is dependent on IL-21 signaling to mediate cytotoxic reprogramming of PD-1 + CD8+ T cells. Nat Immunol [Internet]. Nat Immunol; 2025 [cited 2025 Apr 8];26. https://doi.org/10.1038/S41590-024-02027-0
4. Sade-Feldman M, Yizhak K, Bjorgaard SL, Ray JP, de Boer CG, Jenkins RW, et al. Defining T Cell States Associated with Response to Checkpoint Immunotherapy in Melanoma. Cell. 2018;175:998–e101320. https://doi.org/10.1016/j.cell.2018.10.038.
5. Johnson DB, Estrada MV, Salgado R, Sanchez V, Doxie DB, Opalenik SR et al. Melanoma-specific MHC-II expression represents a tumour-autonomous phenotype and predicts response to anti-PD-1/PD-L1 therapy. Nature Communications 2016 7:1 [Internet]. Nature Publishing Group; 2016 [cited 2024 Jun 3];7:1–10. https://doi.org/10.1038/ncomms10582
6. Ribas A, Wolchok JD. Cancer immunotherapy using checkpoint blockade. Science. 1979;359:1350–5. https://doi.org/10.1126/SCIENCE.AAR4060/ASSET/97E659F6-3962-4E23-AF15-0FD114953352/ASSETS/GRAPHIC/359_1350_F3.JPEG. [Internet]. American Association for the Advancement of Science; 2018 [cited 2024 Jun 3].
7. Tirosh I, Izar B, Prakadan SM, Wadsworth MH, Treacy D, Trombetta JJ et al. Dissecting the multicellular ecosystem of metastatic melanoma by single-cell RNA-seq. Science (1979) [Internet]. American Association for the Advancement of Science; 2016 [cited 2023 Aug 7];352:189–96. https://doi.org/10.1126/SCIENCE.AAD0501/SUPPL_FILE/TIROSH.SM.PDF
8. Sharma P, Hu-Lieskovan S, Wargo JA, Ribas A. Primary, Adaptive, and Acquired Resistance to Cancer Immunotherapy. Cell Cell Press. 2017;168:707–23. https://doi.org/10.1016/J.CELL.2017.01.017.
9. Postow MA, Sidlow R, Hellmann MD. Immune-Related Adverse Events Associated with Immune Checkpoint Blockade. New England Journal of Medicine [Internet]. Massachusetts Medical Society; 2018 [cited 2025 Oct 8];378:158–68. https://doi.org/10.1056/NEJMRA1703481
10. Fridman WH, Pagès F, Saut̀s-Fridman C, Galon J. The immune contexture in human tumours: Impact on clinical outcome. Nat Rev Cancer [Internet] Nat Publishing Group. 2012;12:298–306. https://doi.org/10.1038/NRC3245;SUBJMETA. [cited 2025 Oct 8];.
11. Cassetta L, Pollard JW. Targeting macrophages: Therapeutic approaches in cancer. Nat Rev Drug Discov [Internet]. Nature Publishing Group; 2018 [cited 2025 Oct 8];17:887–904.

https://doi.org/10.1038/NRD.2018.169;SUBJMETA

12. Bied M, Ho WW, Ginhoux F, Blériot C. Roles of macrophages in tumor development: a spatiotemporal perspective. Cellular & Molecular Immunology 2023 20:9 [Internet]. Nature Publishing Group; 2023 [cited 2026 Mar 25];20:983–92. https://doi.org/10.1038/s41423-023-01061-6
13. Xiong D, Wang Y, You M. A gene expression signature of TREM2hi macrophages and γδ T cells predicts immunotherapy response. Nature Communications 2020 11:1 [Internet]. Nature Publishing Group; 2020 [cited 2024 May 27];11:1–12. https://doi.org/10.1038/s41467-020-18546-x
14. Jaitin DA, Adlung L, Thaiss CA, Weiner A, Li B, Descamps H, et al. Lipid-Associated Macrophages Control Metabolic Homeostasis in a Trem2-Dependent Manner. Cell Cell Press. 2019;178:686–e69814. https://doi.org/10.1016/J.CELL.2019.05.054.
15. Ma R-Y, Black A, Qian B-Z. Macrophage diversity in cancer revisited in the era of single-cell omics. Trends Immunol. 2022;43:546–63. https://doi.org/10.1016/j.it.2022.04.008.
16. Tsoi J, Robert L, Paraiso K, Galvan C, Sheu KM, Lay J, et al. Multi-stage Differentiation Defines Melanoma States with Differential Vulnerability to Drug-Induced Iron-Dependent Oxidative Stress. Cancer Cell [Internet] Cancer Cell. 2018;33:890–e9045. https://doi.org/10.1016/J.CCELL.2018.03.017. [cited 2024 May 16];.
17. Satija R, Farrell JA, Gennert D, Schier AF, Regev A. Spatial reconstruction of single-cell gene expression data. Nature Biotechnology. 2015 33:5 [Internet]. Nature Publishing Group; 2015 [cited 2024 May 31];33:495–502. https://doi.org/10.1038/nbt.3192
18. Andreatta M, Carmona SJ, UCell. Robust and scalable single-cell gene signature scoring. Comput Struct Biotechnol J Elsevier. 2021;19:3796–8. https://doi.org/10.1016/J.CSBJ.2021.06.043.
19. Kueckelhaus J, Frerich S, Kada-Benotmane J, Koupourtidou C, Ninkovic J, Dichgans M et al. Inferring histology-associated gene expression gradients in spatial transcriptomic studies. Nature Communications 2024 15:1 [Internet]. Nature Publishing Group; 2024 [cited 2025 Feb 12];15:1–19. https://doi.org/10.1038/s41467-024-50904-x
20. Francis K, Palsson BO. Effective intercellular communication distances are determined by the relative time constants for cyto/chemokine secretion and diffusion. Proc Natl Acad Sci U S A [Internet]. The National Academy of Sciences of the USA; 1997 [cited 2024 Jun 3];94:12258–62. https://doi.org/10.1073/PNAS.94.23.12258/ASSET/9FCEA2F0-1E16-4E00-9F15-60D84AE2B7DB/ASSETS/GRAPHIC/PQ2272845004.JPEG
21. Jin S, Guerrero-Juarez CF, Zhang L, Chang I, Ramos R, Kuan CH et al. Inference and analysis of cell-cell communication using CellChat. Nature Communications 2021 12:1 [Internet]. Nature Publishing Group; 2021 [cited 2024 May 22];12:1–20. https://doi.org/10.1038/s41467-021-21246-9
22. Windhager J, Zanotelli VRT, Schulz D, Meyer L, Daniel M, Bodenmiller B et al. An end-to-end workflow for multiplexed image processing and analysis. Nature Protocols 2023 18:11 [Internet]. Nature Publishing Group; 2023 [cited 2025 Feb 12];18:3565–613. https://doi.org/10.1038/s41596-023-00881-0

23. Stirling DR, Swain-Bowden MJ, Lucas AM, Carpenter AE, Cimini BA, Goodman A. CellProfiler 4: improvements in speed, utility and usability. BMC Bioinformatics [Internet]. BioMed Central Ltd; 2021 [cited 2025 Feb 12];22:1–11. https://doi.org/10.1186/S12859-021-04344-9/FIGURES/6
24. Greenwald NF, Miller G, Moen E, Kong A, Kagel A, Dougherty T et al. Whole-cell segmentation of tissue images with human-level performance using large-scale data annotation and deep learning. Nature Biotechnology. 2021 40:4 [Internet]. Nature Publishing Group; 2021 [cited 2025 Feb 12];40:555–65. https://doi.org/10.1038/s41587-021-01094-0
25. Sequeira AM, Ijsselsteijn ME, Rocha M, de Miranda NFCC. PENGUIN: A rapid and efficient image preprocessing tool for multiplexed spatial proteomics. Comput Struct Biotechnol J [Internet]. 2024;23:3920. https://doi.org/10.1016/J.CSBJ.2024.10.048. [cited 2025 Feb 12];.
26. Giesen C, Wang HAO, Schapiro D, Zivanovic N, Jacobs A, Hattendorf B et al. Highly multiplexed imaging of tumor tissues with subcellular resolution by mass cytometry. Nature Methods 2014 11:4 [Internet]. Nature Publishing Group; 2014 [cited 2025 Feb 12];11:417–22. https://doi.org/10.1038/nmeth.2869
27. Hugo W, Zaretsky JM, Sun L, Song C, Moreno BH, Hu-Lieskovan S, et al. Genomic and Transcriptomic Features of Response to Anti-PD-1 Therapy in Metastatic Melanoma. Cell. 2016;165:35–44. https://doi.org/10.1016/j.cell.2016.02.065.
28. Riaz N, Havel JJ, Makarov V, Desrichard A, Urba WJ, Sims JS, et al. Tumor and Microenvironment Evolution during Immunotherapy with Nivolumab. Cell Cell Press. 2017;171:934–e94916. https://doi.org/10.1016/J.CELL.2017.09.028.
29. Van Allen EM, Miao D, Schilling B, Shukla SA, Blank C, Zimmer L et al. Genomic correlates of response to CTLA-4 blockade in metastatic melanoma. Science (1979). 2015;350:207–11. https://doi.org/10.1126/science.aad0095
30. Liu D, Schilling B, Liu D, Sucker A, Livingstone E, Jerby-Arnon L, et al. Integrative molecular and clinical modeling of clinical outcomes to PD1 blockade in patients with metastatic melanoma. Nat Med. 2019;25:1916–27. https://doi.org/10.1038/s41591-019-0654-5.
31. Gide TN, Quek C, Menzies AM, Tasker AT, Shang P, Holst J, et al. Distinct Immune Cell Populations Define Response to Anti-PD-1 Monotherapy and Anti-PD-1/Anti-CTLA-4 Combined Therapy. Cancer Cell. 2019;35:238–e2556. https://doi.org/10.1016/j.ccell.2019.01.003.
32. Freeman SS, Sade-Feldman M, Kim J, Stewart C, Gonye ALK, Ravi A, et al. Combined tumor and immune signals from genomes or transcriptomes predict outcomes of checkpoint inhibition in melanoma. Cell Rep Med. 2022;3:100500. https://doi.org/10.1016/j.xcrm.2021.100500.
33. Freeman SS, Sade-Feldman M, Kim J, Stewart C, Gonye ALK, Ravi A, et al. Combined tumor and immune signals from genomes or transcriptomes predict outcomes of checkpoint inhibition in melanoma. Cell Rep Med Cell Press. 2022;3:100500. https://doi.org/10.1016/J.XCRM.2021.100500.
34. Wiens M, Verone-Boyle A, Henscheid N, Podichetty JT, Burton J. A Tutorial and Use Case Example of the eXtreme Gradient Boosting (XGBoost) Artificial Intelligence Algorithm for Drug Development

Applications. Volume 18. John Wiley and Sons Inc; 2025. p. e70172. [cited 2026 Apr 8];. https://doi.org/10.1111/CTS.70172. Clin Transl Sci [Internet].

35. Xiong D, Wang Y, You M. A gene expression signature of TREM2 hi macrophages and γδ T cells predicts immunotherapy response. [cited 2023 Oct 17]; https://doi.org/10.1038/s41467-020-18546-x
36. Andreatta M, Carmona SJ, UCell. Robust and scalable single-cell gene signature scoring. Comput Struct Biotechnol J. 2021;19:3796–8. https://doi.org/10.1016/j.csbj.2021.06.043.
37. Chen B, Khodadoust MS, Liu CL, Newman AM, Alizadeh AA. Profiling Tumor Infiltrating Immune Cells with CIBERSORT. 2018. pp. 243–59. https://doi.org/10.1007/978-1-4939-7493-1_12
38. Mulder K, Patel AA, Kong WT, Piot C, Halitzki E, Dunsmore G, et al. Cross-tissue single-cell landscape of human monocytes and macrophages in health and disease. Immunity. 2021;54:1883–e1900. https://doi.org/10.1016/j.immuni.2021.07.007. 5.
39. Massier L, Jalkanen J, Elmastas M, Zhong J, Wang T, Nono Nankam PA, et al. An integrated single cell and spatial transcriptomic map of human white adipose tissue. Nat Commun [Internet] Nat Res. 2023;14:1–19. https://doi.org/10.1038/S41467-023-36983-2;TECHMETA. [cited 2025 Sep 9];.
40. Vahid MR, Brown EL, Steen CB, Zhang W, Jeon HS, Kang M et al. High-resolution alignment of single-cell and spatial transcriptomes with CytoSPACE. Nature Biotechnology 2023 41:11 [Internet]. Nature Publishing Group; 2023 [cited 2025 Feb 12];41:1543–8. https://doi.org/10.1038/s41587-023-01697-9
41. Francis K, Palsson BO. Effective intercellular communication distances are determined by the relative time constants for cyto/chemokine secretion and diffusion. Proc Natl Acad Sci U S A [Internet]. 1997 [cited 2025 Apr 9];94:12258. https://doi.org/10.1073/PNAS.94.23.12258
42. Jaitin DA, Adlung L, Thaiss CA, Weiner A, Li B, Descamps H, et al. Lipid-Associated Macrophages Control Metabolic Homeostasis in a Trem2-Dependent Manner. Cell [Internet] Cell Press. 2019;178:686–e69814. https://doi.org/10.1016/J.CELL.2019.05.054. [cited 2025 Oct 8];.
43. Wenes M, Shang M, Di Matteo M, Goveia J, Martín-Pérez R, Serneels J et al. Macrophage Metabolism Controls Tumor Blood Vessel Morphogenesis and Metastasis. Cell Metab [Internet]. Cell; 2016 [cited 2025 Oct 8];24:701–15. https://doi.org/10.1016/J.CMET.2016.09.008
44. Jin R, Neufeld L, McGaha TL. Linking macrophage metabolism to function in the tumor microenvironment. Nature Cancer 2025 [Internet]. Nature Publishing Group; 2025 [cited 2025 Feb 19];1–14. https://doi.org/10.1038/s43018-025-00909-2
45. Redondo-Muñoz M, Rodriguez-Baena FJ, Aldaz P, Caballé-Mestres A, Moncho-Amor V, Otaegi-Ugartemendia M, et al. Metabolic rewiring induced by ranolazine improves melanoma responses to targeted therapy and immunotherapy. Nat Metab [Internet] Nat Metab. 2023;5:1544–62. https://doi.org/10.1038/S42255-023-00861-4. [cited 2026 Apr 14];.
46. Timperi E, Gueguen P, Molgora M, Magagna I, Kieffer Y, Lopez-Lastra S et al. Lipid-Associated Macrophages Are Induced by Cancer-Associated Fibroblasts and Mediate Immune Suppression in Breast Cancer. Cancer Res [Internet]. American Association for Cancer Research Inc.; 2022 [cited

2024 May 28];82:3291–306. https://doi.org/10.1158/0008-5472.CAN-22-1427/707127/AM/LIPID-ASSOCIATED-MACROPHAGES-ARE-INDUCED-BY-CANCER.

47. Molgora M, Esaulova E, Vermi W, Hou J, Chen Y, Luo J, et al. TREM2 Modulation Remodels the Tumor Myeloid Landscape Enhancing Anti-PD-1 Immunotherapy. Cell Cell Press. 2020;182:886–e90017. https://doi.org/10.1016/J.CELL.2020.07.013.
48. Adaku N, Ostendorf BN, Mei W, Tavazoie SF, Apolipoprotein E, American Association for Cancer Research Inc.. 2 Stimulates Protein Synthesis and Promotes Melanoma Progression and Metastasis. Cancer Res [Internet]. ; 2023 [cited 2024 May 22];83:3013–25. https://doi.org/10.1158/0008-5472.CAN-23-1252/727339/AM/APOLIPOPROTEIN-E2-STIMULATES-PROTEIN-SYNTHESIS-AND
49. Bugler-Lamb A, Guilliams M. Myeloid Cells TREM Down Anti-tumor Responses. Cell Cell Press. 2020;182:796–8. https://doi.org/10.1016/J.CELL.2020.07.042.
50. Jarnicki AG, Lysaght J, Todryk S, Mills KHG. Suppression of Antitumor Immunity by IL-10 and TGF-β-Producing T Cells Infiltrating the Growing Tumor: Influence of Tumor Environment on the Induction of CD4 + and CD8 + Regulatory T Cells. The Journal of Immunology [Internet]. American Association of Immunologists; 2006 [cited 2025 Feb 19];177:896–904. https://doi.org/10.4049/JIMMUNOL.177.2.896
51. Molgora M, Esaulova E, Vermi W, Hou J, Chen Y, Luo J, et al. TREM2 Modulation Remodels the Tumor Myeloid Landscape Enhancing Anti-PD-1 Immunotherapy. Cell Cell Press. 2020;182:886–e90017. https://doi.org/10.1016/J.CELL.2020.07.013.
52. Tumeh PC, Harview CL, Yearley JH, Shintaku IP, Taylor EJM, Robert L et al. PD-1 blockade induces responses by inhibiting adaptive immune resistance. Nature 2014 515:7528 [Internet]. Nature Publishing Group; 2014 [cited 2024 May 28];515:568–71. https://doi.org/10.1038/nature13954
53. Spranger S, Spaapen RM, Zha Y, Williams J, Meng Y, Ha TT et al. Up-regulation of PD-L1, IDO, and Tregs in the melanoma tumor microenvironment is driven by CD8 + T cells. Sci Transl Med [Internet]. American Association for the Advancement of Science; 2013 [cited 2024 May 28];5. https://doi.org/10.1126/SCITRANSLMED.3006504/SUPPL_FILE/5-200RA116_SM.PDF
54. Mariathasan S, Turley SJ, Nickles D, Castiglioni A, Yuen K, Wang Y et al. TGFβ attenuates tumour response to PD-L1 blockade by contributing to exclusion of T cells. Nature 2018 554:7693 [Internet]. Nature Publishing Group; 2018 [cited 2025 Feb 12];554:544–8. https://doi.org/10.1038/nature25501
55. Rosenbaum SR, Wilski NA, Aplin AE. Fueling the fire: Inflammatory forms of cell death and implications for cancer immunotherapy. Cancer Discov [Internet]. Volume 11. American Association for Cancer Research Inc.; 2021. p. 266. [cited 2025 Feb 12];. https://doi.org/10.1158/2159-8290.CD-20-0805.
56. Sadrolashrafı K, Samlowski W. Retreatment of Patients With Metastatic Cutaneous Melanoma Who Relapse After Elective Checkpoint Inhibitor Discontinuation After a Complete Remission. Oncologist [Internet]. Oxford Academic; 2023 [cited 2025 Mar 28];28:e270–5. https://doi.org/10.1093/ONCOLO/OYAD016

Figures

Fig. 1

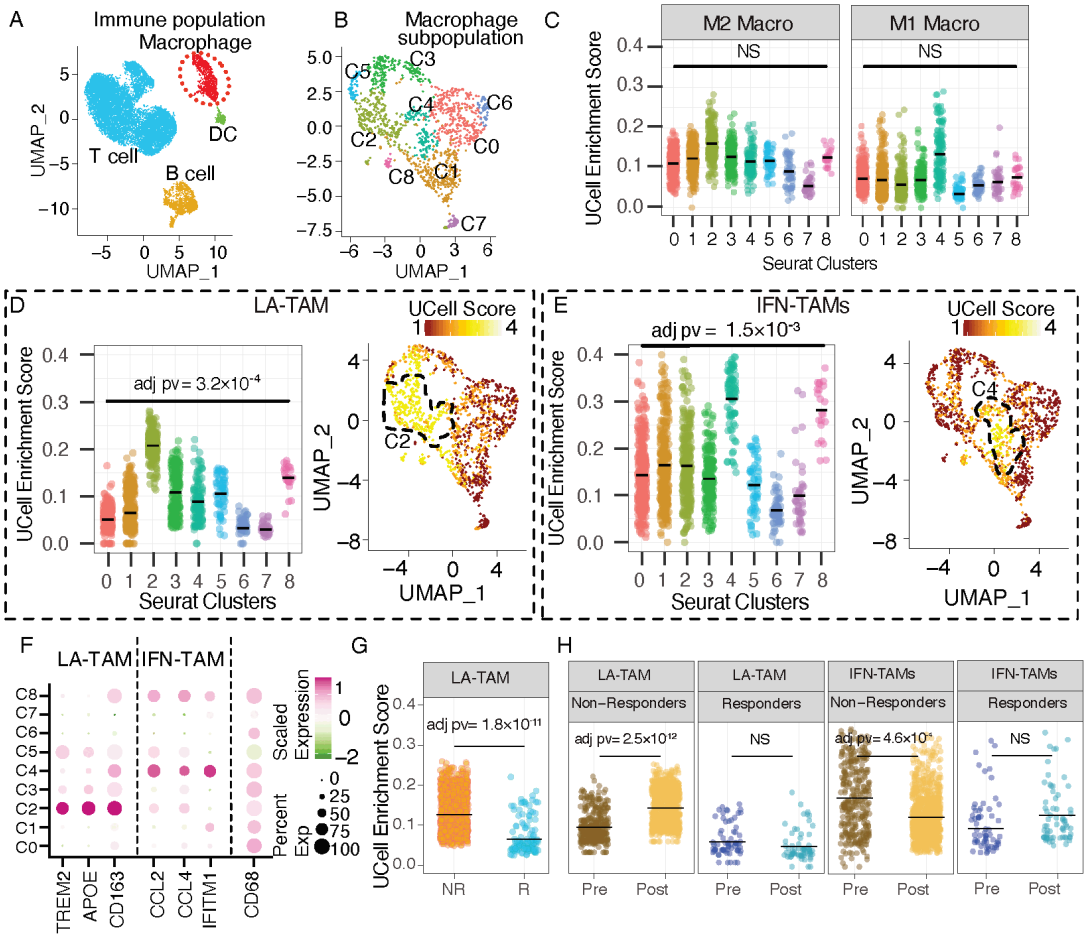


Figure 1

Lipid associated TAM (LA-TAM) population is enriched in ICI Non-Responder melanoma patients

(A) UMAP clustering of the $CD45^{+}$ immune cells (N= 16,291) from 32 patients (retrieved from Sade-Feldman *et al.*[4]), where the macrophage population is highlighted by a red dashed circle. (B) The macrophage population was subjected to Louvain clustering analysis, which resulted in 9 clusters (C0-C8) representing different subpopulations of macrophages. Color code represents different clusters. (C) Single-cell UCell enrichment scores of the gene signatures representing M2 and M1 macrophages are shown as a jitter plot. Adjusted p-value is calculated across the Seurat Clusters (NS = non-significant, adjusted p-value > 0.05). (D) UCell enrichment score for the LA-TAM gene signature is represented as a jitter plot (left) and UMAP (right). The UMAP shows the scaled UCell scores where the C2 population is demarked by a black dashed line. (E) UCell enrichment score for IFN-TAM gene signature is represented as a jitter plot (left) and UMAP (right). The UMAP shows the scaled UCell scores where the C4 population is demarked by a black dashed line. (F) Dot plot showing the cluster-wise expression of marker genes defining LA-TAM (TREM2, APOE, and CD163), IFN-TAM (CCL2, CCL4, IFITM1), and macrophage (CD68). Color code indicates expression levels, and circle size defines percent of cells expressing the genes. (G) Single-cell-wise UCell enrichment scores for the LA-TAM state between Non-Responder (NR) and Responder (R) patients are shown. Significant adjusted p-value (adj pv= $1.8´10^{-11}$) is indicated. (H) UCell enrichment scores for two TAM states (LA-TAM and IFN-TAM) between pre- (Pre) and post-treatment (Post) time points across Non-Responder and Responder melanoma patients are shown. Significant adj p-values are given. (NS represents a not-significant p-value).

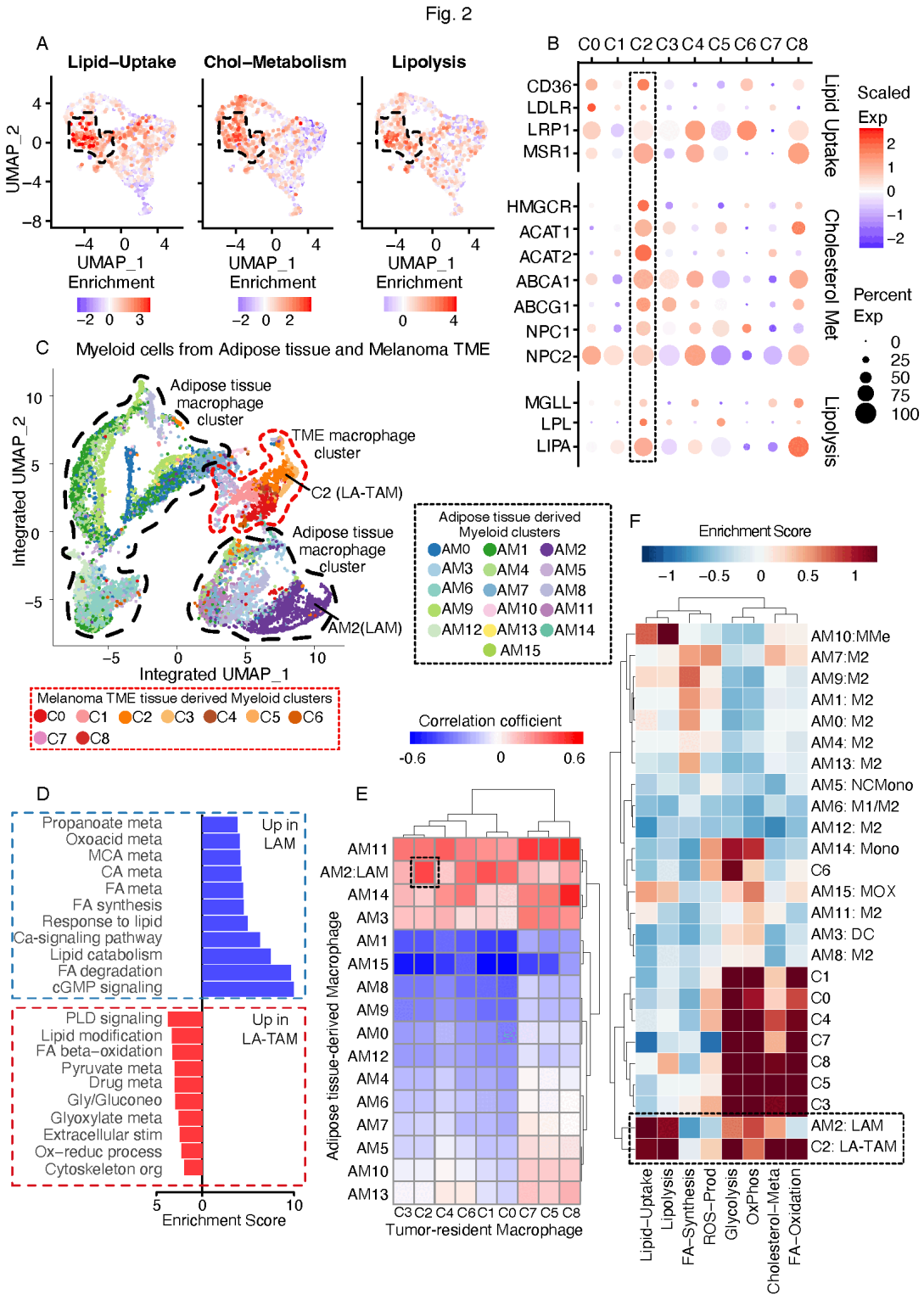


Figure 2

Similarities and differences between tumor-resident LA-TAMs and adipose tissue-derived LAMs

(A) Enrichment of lipid metabolism-associated gene sets (Lipid-Uptake, Cholesterol (Chol) Metabolism, and Lipolysis) across the macrophage population. Enrichment based on the Univariate Linear Model (ULM) is mapped in UMAP space. Color code represents the Enrichment score. (B) Scaled gene

expressions associated with Lipid-Uptake, Cholesterol Metabolism, and Lipolysis across Seurat clusters of macrophage population are shown as a dot plot. Color code indicates expression levels, and circle size defines percent of cells expressing the genes. (C) Integrated UMAP of macrophage populations from melanoma TME and Adipose tissue. Sixteen Adipose tissue-derived macrophage clusters are denoted as AM0-AM15 (Adipose-macrophage), whereas Nine Tumor-resident Macrophage clusters are simply denoted as “C0-C8”. C2 and AM2 are denoted as LA-TAM and LAM, respectively. (D) Pathway enrichment scores (-log10Adj.pv) of differentially expressed genes between LA-TAMs and LAMs are shown. (E) Transcriptional concordances (Spearman's rank correlation coefficient) between Tumor-resident Macrophages and Adipose tissue-derived Macrophages are shown as a color code. (F) Enrichment of lipid metabolism associated pathways across Tumor-resident Macrophages and Adipose tissue-derived Macrophages. Color code represents the Enrichment score.

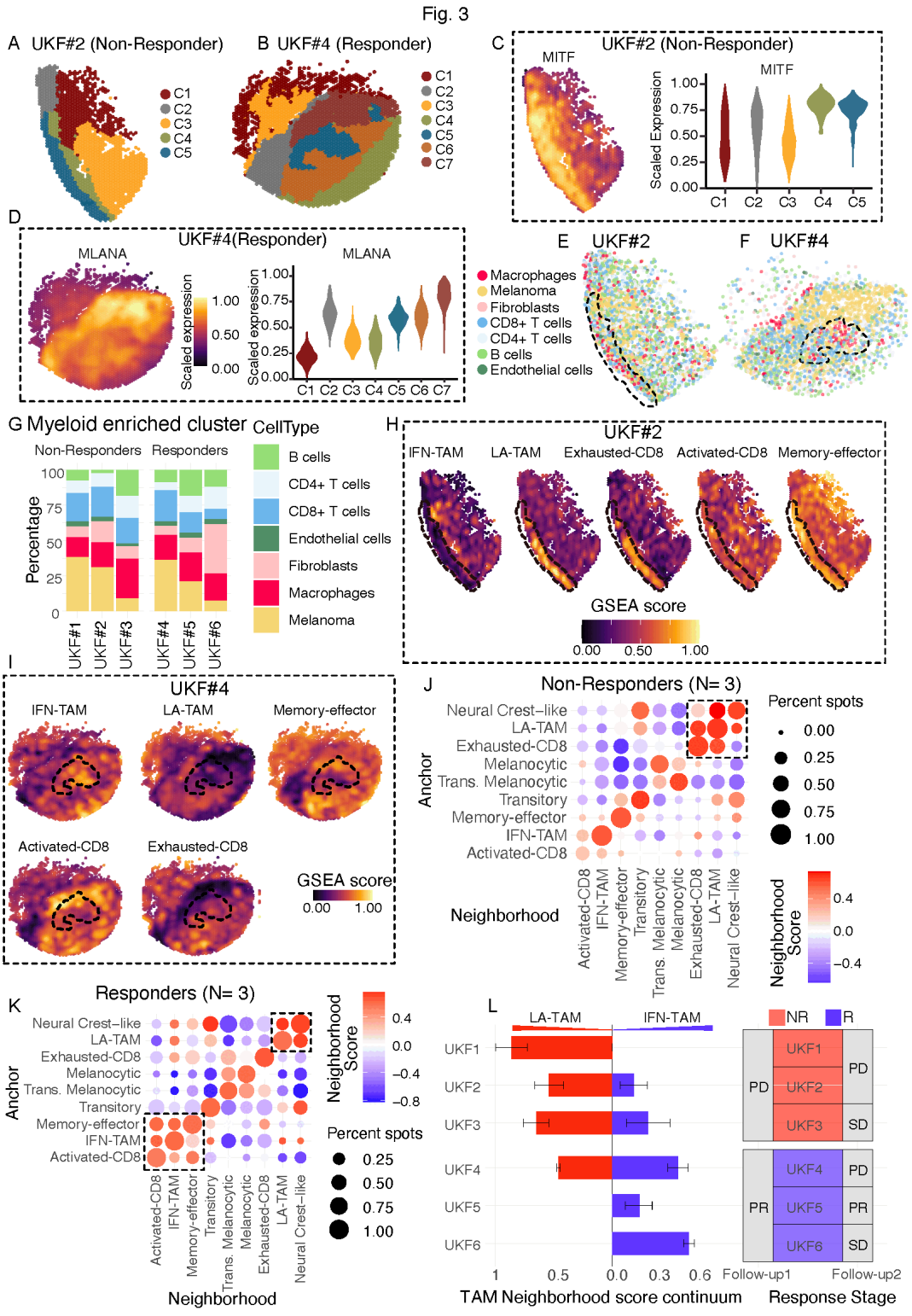


Figure 3

Spatial colocalization of contrasting states of TAMs and CD8$^+$ T cells in Non-Responder and Responder patients

BayesSpace clustering based on the spatial transcriptome data from UKF#2 (A) and UKF#4 (B). (C) For UKF#2, the scaled expression of the canonical melanoma marker (MITF) is shown as a surface

expression and violin plots. The color code of the surface plot represents the relative gene expression. The cluster-wise expression of MITF is depicted in a violin plot. (D) For UKF#4, the scaled expression of canonical melanoma markers (MLANA) is shown as a surface expression plot where the color code represents the relative gene expression. In addition, the cluster-wise expression of MLANA is depicted in a violin plot. (E, F) Deconvolution of spatial spots was performed in UKF#2 (E) and UKF#4 (F) by assigning single-cell transcriptome profiles [7] where different colors represent distinct cell types (Macrophages, Melanoma, Fibroblast, $CD8^+$ T cell, $CD4^+$ T cell, B cell, and Endothelial cells). The spatial boundary demarketing C5 region is shown by a black dashed line for both tissues. The C5 spatial regions of UKF#2 (E) and UKF#4 (F) are annotated as a “Myeloid-enriched region”. (G) The percentages of different cell types in the Myeloid-enriched region are shown as stacked bar plots across the Non-Responder and Responder tissues. (H and I), Enrichments of selected gene signatures representing IFN-TAMs, LA-TAMs, Exhausted-CD8 T cells, Activated CD8, and Memory-effector T cells are illustrated by surface plots for UKF#2 (H) and for UKF#4 (I). The GSEA score is depicted by color code. Myeloid-enriched regions (C5) are marked with dashed lines for tissue sections. (J and K) Neighborhood analysis was performed to quantify the distance among the spots enriched with two different gene signatures and estimate the spatial co-localization probability of the gene signatures. The results are represented as dot plots for all three Non-Responder (J) and three Responder (K) patients. The gene sets in the rows are anchors signifying that spatially enriched spots are selected with respect to these anchor gene signatures (rows), and the columns indicate the neighborhood corresponding to the spatial overlap of these gene signatures. The higher positive score (red) indicates the co-localization, whereas the lower negative score (blue) indicates that the gene signatures are distinctly located (non-overlapping). Percent spots represent the fraction of colocalized spots between two gene signatures. (L) LA-TAM and IFN-TAM neighborhood scores per patient are illustrated as bar plots. ICI therapy response status of each patient based on iRECIST (immune-Related Response Criteria) is shown for two time points (Follow-up1 and Follow-up2).

Fig. 4

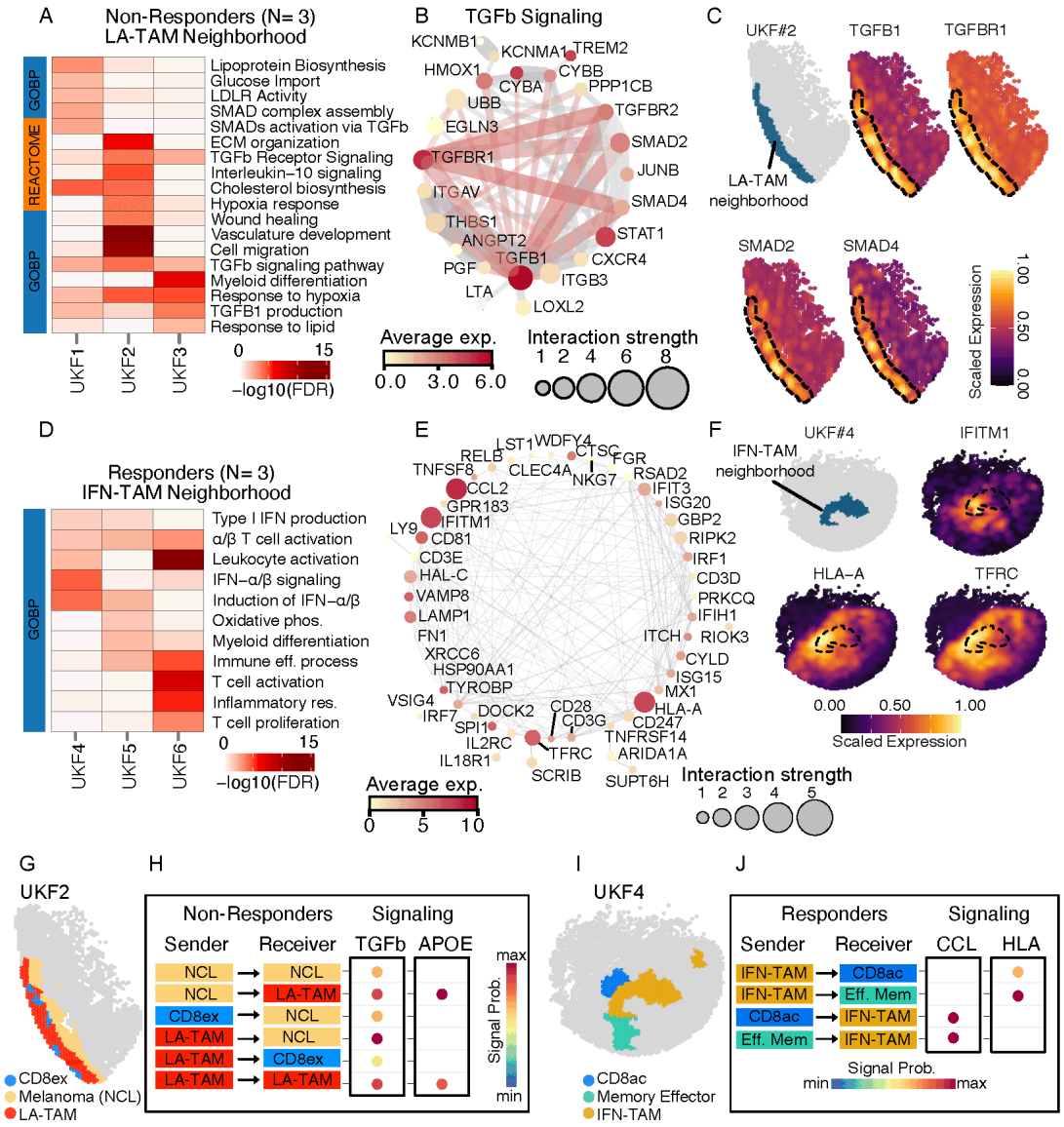


Figure 4

Functionally opposing signaling pathways enriched in LA-TAM and IFN-TAM neighborhoods

(A) Pathway enrichment of the differentially expressed genes (DEGs) in the LA-TAM neighborhoods across Non-Responders (UKF#1, UKF#2, UKF#3). Color code shows -log10FDR values. GOBP (Gene Ontology Biological Process) and REACTOME gene sets are highlighted as different color. (B) The

signaling network of TGFb-signaling is shown in the LA-TAM neighborhood of Non-Responders, where the node color shows the average expression of genes in the LA-TAM neighborhood. The size of the node represents the interaction strength. The width of nodes represents the probability of PPI interactions, whereas the red colored edges represent the connection between the Ligand, receptor, and immediate downstream components of TGFb-signaling. (C) For UKF#2, expression distributions of TGFb-signaling genes are illustrated by surface plots where scaled gene expression is depicted by color code. The LA-TAM neighborhood is marked by dashed lines within tissue sections. (D) GOBP Enrichment of the differentially expressed genes of IFN-TAM neighborhood across Responder patients (UKF#4, UKF#5, UKF#6), where color code represents the -log10FDR values. (E) The IFN-signaling network in the IFN-TAM neighborhood of UKF#4 is shown, where the node color shows the log2 FC between the IFN-TAM neighborhood vs. the rest of the tissue. The size of the node represents the number of edges. (F) For UKF#4, expression distributions of IFN-signaling genes are illustrated by surface plots where scaled gene expression is depicted by color code. The IFN-TAM neighborhood is marked by dashed lines within tissue sections. (G) LA-TAM neighborhood composed of spots enriched in LA-TAM, Exhausted-CD8 T cells (CD8ex) and Neural crest-like Melanoma cells (NCL) are defined (GSEA score above the median) across Non-Responder samples. As an exemplar, LA-TAM, CD8ex and NCL (Melanoma) enriched spots in UKF#2 is shown. (H) CellChat analysis shows the cell-to-cell communications via TGF-b and APOE-signaling between sender and receiver cells within LA-TAM neighborhoods across Non-Responders is depicted as a dot plot. The color code represents the signaling probability. (I) Similarly, the IFN-TAM neighborhood is defined by the adjacent tissue regions enriched in IFN-TAM, Activated-CD8 T cells, and Memory Effector cells. Pre-defined IFN-TAM neighborhood in UKF#4 sample is shown. (J) Cell-to-cell communications via CCL and HLA signaling within IFN-TAM neighborhood across Responders are shown. Like before, the color code indicates the probability of signaling.

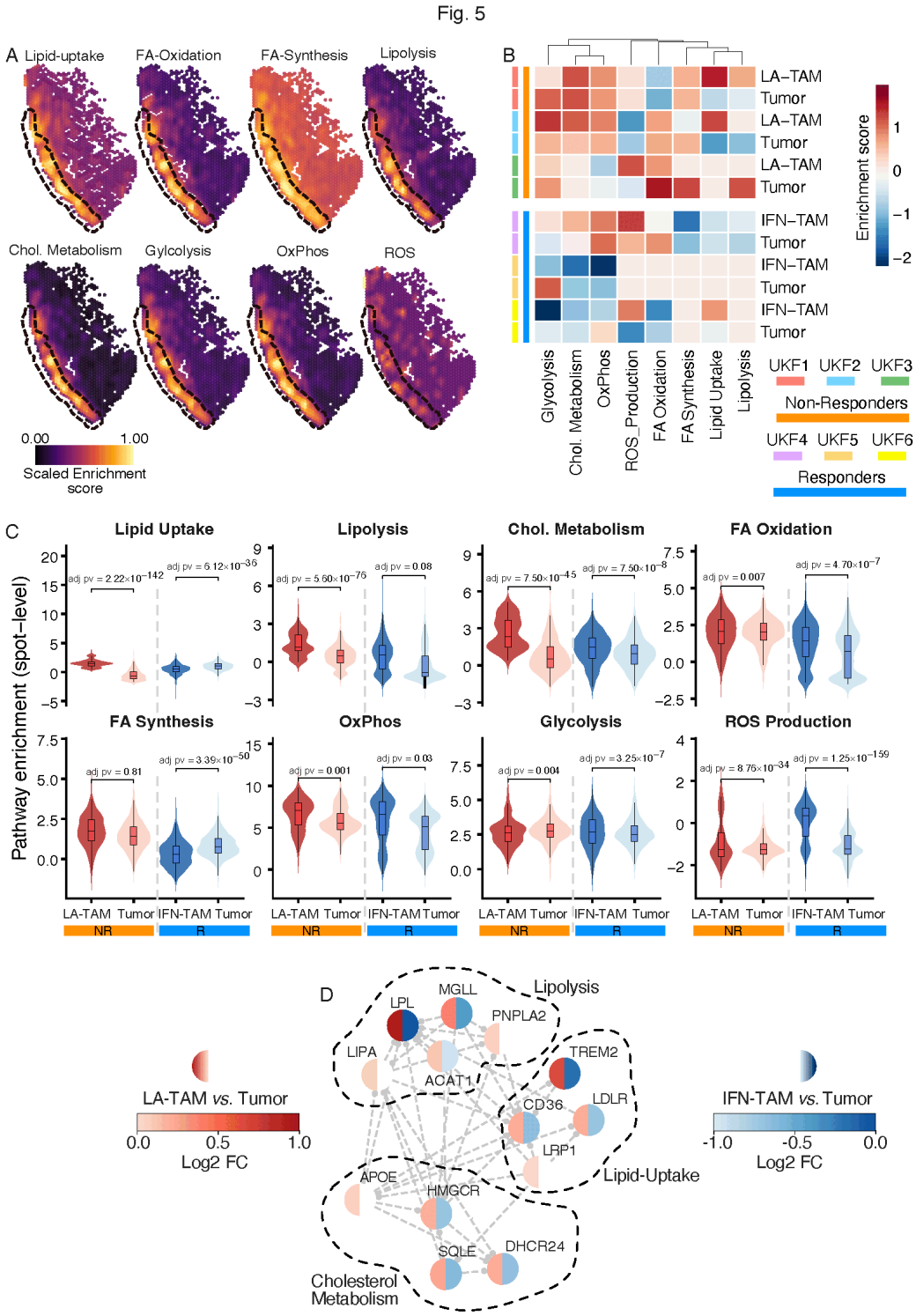


Figure 5

Spatial distribution of Lipid Metabolism associated pathways between Non-Responders and Responders

(A) Surface plot showing enrichment of gene sets associated Lipid Metabolism in the Non-Responder sample UKF#2. The scaled enrichment score is defined by color code. The black dashed line represents

the LA-TAM region within the tissue. (B) Enrichment of pre-selected gene sets associated with Lipid Metabolic processes across Non-Responder and Responder samples is shown. Within tissue, TAM-neighborhoods (LA-TAM in Non-Responder and IFN-TAM in Responder samples) and tumor regions were selected for enrichment. The color scale indicates the differential enrichment scores. (C) Comparison of enrichment score of lipid metabolic gene sets between the different tissue regions of the same tissue. Adjusted P-value is calculated by Mixed-Effects Modeling of Gene-Set Activity. The adj pv values are indicated where appropriate. (D) Fold changes of genes associated with Lipid-Uptake, Lipolysis, and Cholesterol Metabolism between LA-TAM/IFN-TAM and adjacent tumor regions across Non-Responder and Responder samples are illustrated in a PPI network plot. Red and blue color gradients represent the fold change of LA-TAM vs. Tumor and IFN-TAM vs. Tumor, respectively. The grey dashed line indicates the interaction potential of proteins.

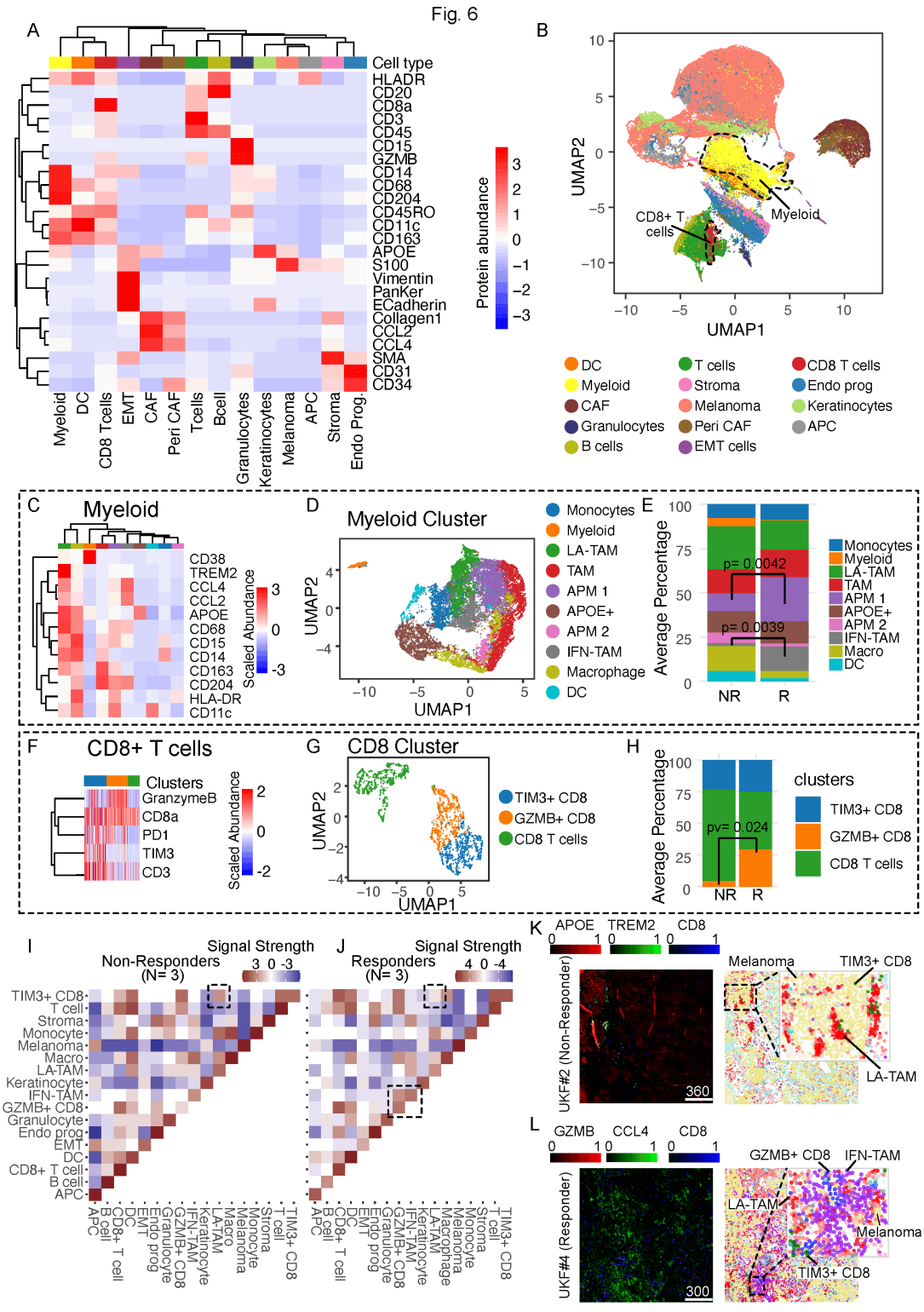


Figure 6

Imaging mass cytometry analysis of immune and tumor microenvironment heterogeneity in metastatic melanoma patients.

(A) Multiparametric imaging mass cytometry (IMC) was performed on tissue samples from metastatic melanoma patients. Heatmap showing the scaled (row) protein abundance of selected immune, stromal,

and tumor markers across different cell types identified in the tumor microenvironment. Both column and row Hierarchical clustering based on Euclidean distance was applied. Cell annotation was performed based on the expression of cell-type-specific markers. (B) UMAP representation of single-cell IMC data, illustrating the distribution of major cell types, including myeloid cells, $CD8^+$ T cells, stromal cells, and melanoma cells. Myeloid and $CD8^+$ T cell populations were highlighted by a dashed line. These cell populations were selected for further analysis. (C) Heatmap of scaled protein expression in the myeloid compartment, highlighting differentially abundant markers across 10 clusters. Cell annotations were based on the expression of canonical markers (eg, concurrent expression of APOE and TREM2, and CD163 was considered as the signature of LA-TAM cells; similarly, expression of CCL2 and CCL2, along with macrophage marker CD68, was considered as the defining feature of IFN-TAM). (D) UMAP clustering of myeloid cells, identifying distinct subpopulations, including LA-TAM and IFN-TAM. (E) Bar graph comparing the proportional distribution of myeloid cell subsets between Non-Responders (NR) and Responders (R), showing a significant proportional difference of IFN-TAM (pv = 0.0039). (F) Heatmap showing marker expression profiles of $CD8^+$ T cell subsets, including TIM^+ $CD8^+$ T cells and $GZMB^+$ $CD8^+$ T cells. (G) UMAP clustering of $CD8^+$ T cells, distinguishing functionally distinct subsets based on protein expression. (H) The proportions of $CD8^+$ T cell subsets in Non-Responders and Responders are shown. Significant p-value (pv) is given (pv = 0.024). (I, J) Heatmaps depicting the probability of intercellular interactions within a spatial neighborhood across all three Non-Responder (I) and three Responder (J) patients. Signal strength representing the probability of interaction in the neighborhood microenvironment was shown as a color code. The dashed boxes highlight differences in interactions involving different TAM and $CD8^+$ cell states. (K) Representative IMC image of a Non-Responder sample (UKF#2), showing the spatial distribution of APOE, TREM2, and TIM^+ CD8 T cells in relation to LA-TAM cells (K). (L) Representative IMC image of a Responder sample (UKF#4), showing GZMB, CCL4, and $CD8^+$ T cells, with distinct localization of IFN-TAM and $GZMB^+$ $CD8^+$ T cells. Scale is given in mm.

Fig. 7

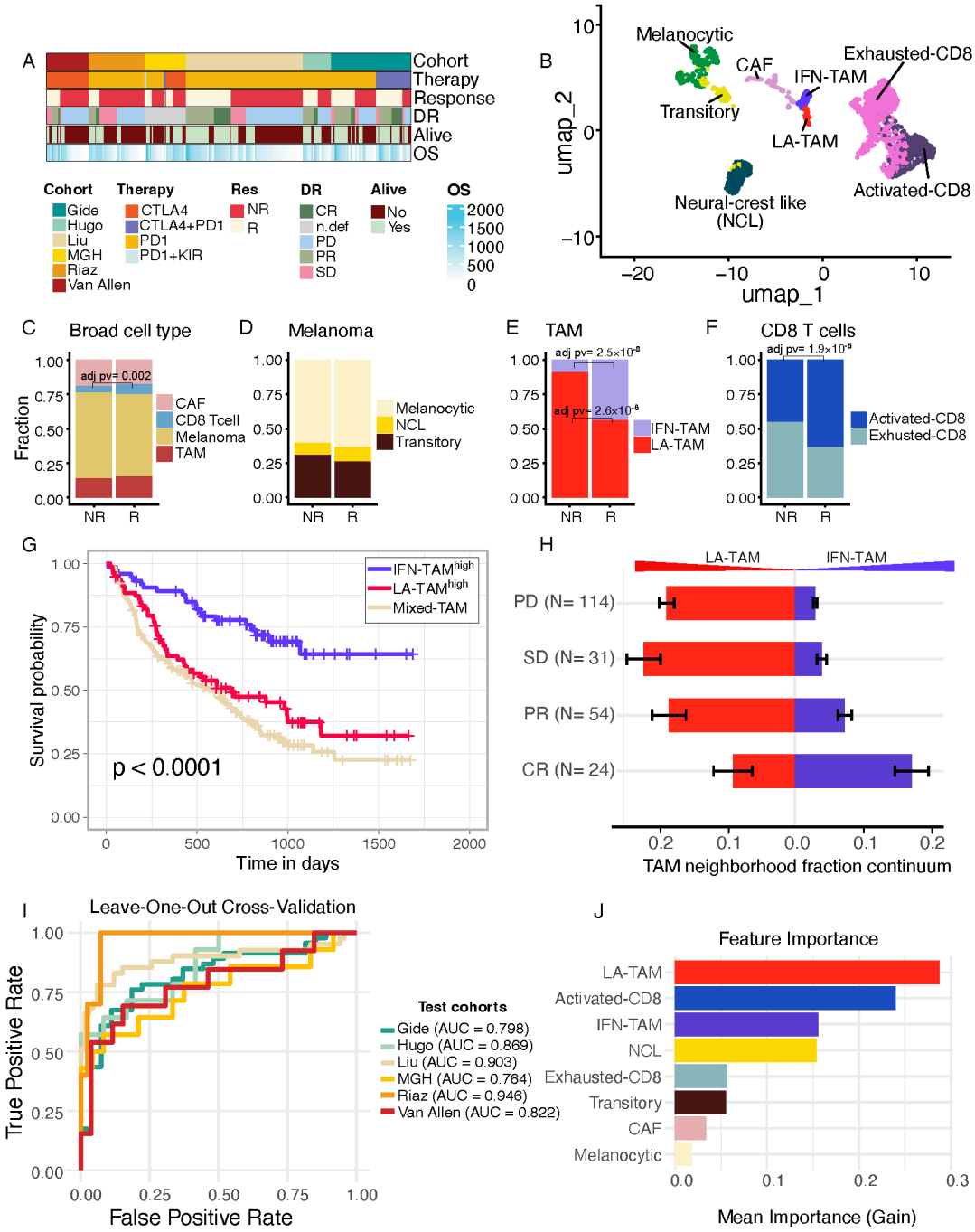


Figure 7

Validation of the association between LA-TAM and poor ICI esponse in large cohort

(A) Bulk RNA-seq and clinical data from treatment naïve (pre-treatment) melanoma patients (N= 334) were collected from six independent cohorts (Gide [31], Hugo [27], Liu [30], MGH [32], Riaz [28], Van Allen [29]. All cohorts bulk RNA-seq data were processed as described by Freeman *et al.* [32]). Different

cohorts, responses, and therapy types are depicted as color codes. (B) UMAP of annotated single cells representing different states of melanoma, TAMs, $CD8^+$ T cells, and CAF. (C) The fractions of the major cell populations (Melanoma, CAF, TAMs, and $CD8^+$ T cells) across the tissue samples between Non-Responders (NR) and Responders (R) melanoma patients from the pretreatment (pre-ICI) cohort (N= 334). Adjusted p-value (adj pv) is shown. (D) Fractions of melanoma states (Melanocytic, NCL, and Transitory) in the pre-ICI cohort were shown in a bar plot. (E) TAM-state fractions were compared between NR and R patients. The adj pvs are shown. (F) Fractions of CD8+ T cell states were compared between NR and R patients. The adj pv is shown. (G) Kaplan Meier curve showing the survival outcome of the pre-stratified patients ($LA\text{-}TAM^{high}$, Mixed-TAM, and $IFN\text{-}TAM^{high}$). (H) LA-TAM and IFN-TAM neighborhood fractions across the detailed response categories (PD, SD, PR, and CR) are illustrated as bar plots. The X-axis is divided into two parts, where the left side shows the LA-TAM neighborhood fraction, whereas the right side represents the IFN-TAM neighborhood fraction. (I) Receiver-operator curves for each validation cohort are shown. AUC of each validation cohort is also given. (J) The mean importance scores of all the features representing the estimated cellular fractions are shown.

Supplementary Files

This is a list of supplementary files associated with this preprint. Click to download.

- Additionalfile1.pdf
- Additionalfile2TableS1.xlsx
- Additionalfile3TableS2.xlsx
- Additionalfile4TableS3.xlsx
- Additionalfile5TableS4.xlsx
- Additionalfile6TableS5.xlsx
- Additionalfile7TableS6.xlsx
- Additionalfile8TableS7.xlsx
- SupplementaryInformation.docx